Contents lists available at ScienceDirect

Arabian Journal of Chemistry

journal homepage: www.ksu.edu.sa

Phase behavior-microstructure-crystallization kinetics correlations in semi-crystalline/amorphous PCL/SAN mixtures filled with nanosilica

Samaneh Salkhi Khasraghi [a,1], Hanieh Khonakdar [b,1], Farkhondeh Hemmati [c,*], Sara Zarei [b], Fatemeh Sadat Miri [b], Marcos A.L. Nobre [d], Hossein Ali Khonakdar [b,*]

[a] Department of Chemical and Petroleum Engineering, Sharif University of Technology, P.O. Box, 11155-9465 Tehran, Iran
[b] Department of Polymer Processing, Iran Polymer and Petrochemical Institute, P.O. Box 14965-115, Tehran, Iran
[c] Caspian Faculty of Engineering, College of Engineering, University of Tehran, P.O. Box 43841-119, Guilan, Iran
[d] São Paulo State University (Unesp), School of Technology and Sciences, Presidente Prudente, SP, 19060-900, Brazil

ARTICLE INFO

Keywords:
Phase behavior
Poly(ε-caprolactone)
Nanocomposite
Blends
Crystallization

ABSTRACT

In this study, the effects of poly(ε-caprolactone) (PCL) molecular weight and the type and presence of nanosilica on the non-isothermal crystallization behavior of PCL in the PCL/poly(styrene-*co*-acrylonitrile) (SAN)/nanosilica systems have been quantitatively investigated. The PCL/SAN system have been chosen as an ideal model system because of the special phase behavior of the blends, which include a lower-critical solution temperature (LCST) phase diagram over a virtual upper-critical solution temperature. By this choose, the great importance of phase separation, mutual phase dissolution and preferential nanoparticle migration to one of the polymeric phases on the crystallization behavior during a commercial production process has been highlighted. The addition of both hydrophilic (Si) and hydrophobic (SiR) silica nanoparticles to virgin PCLs with different molecular weights retards the crystallization process. However, the presence of these nanoparticles in PCL/SAN blends impacts the PCL crystallization kinetics in opposite ways, depending on the nanosilica type, PCL molecular weight and melt cooling rate. The reasons for the observed opposite trends are the changes in the LCST-type phase diagram position by altering the PCL molecular weight and nanosilica type, the selective migration of nanoparticles as well as the dispersion state of nanofillers. The presence of both Si and SiR nanosilicas increases the crystallization activation energy, respectively, by 4.2% and 2.4% for the PCL/SAN blend conatining the PCL with lower molecular weight. While the addition of both Si (11%) and SiR (6.7%) reduces this energy for the blend conatining the PCL with higher molecular weight.

1. Introduction

During the past decades, blending of polymers as an available and popular economical method has been attracted a lot of attention to modify the properties of polymeric products (Higgins et al., 2005; Ghafouri et al., 2022). For partial miscible polymer blends containing a semi-crystalline phase and an amorphous phase, it is possible to study the phase behavior and performance by following the crystallization kinetics of the semi-crystalline phase (Moeinifar et al., 2020). The final properties of polymer blends depend on the properties of their pure components, miscibility and multiphase morphology (Salkhi Khasraghi et al., 2022; Svoboda et al., 1999). Polymer blends including a semi-crystalline poly(ε-caprolactone) (PCL) component and an amorphous phase have been widely studied in recent years (Madbouly and Ougizawa, 2004; Hemmati et al., 2014; Mohtaramzadeh et al., 2020). PCL is an aliphatic and hydrophobic semi-crystalline polyester that is commonly used in biomedical applications such as tissue engineering and drug delivery (Maghoul et al., 2023; Khadivi et al., 2023).

PCL in the molten state is miscible with various polymers, such as poly(styrene-*co*-acrylonitrile) (SAN) and poly(vinyl methyl ether), at the molecular level (Mohamed and Yusoh, 2016; Woodruff and Hutmacher, 2010). Based on the researches, PCL with SAN shows miscible behavior when the copolymer contains 8 to 28 % by weight of acrylonitrile comonomer (Moeinifar et al., 2020; Schulze et al., 1993). In polymer blends containing semi-crystalline/amorphous regions, such as PCL/SAN blends, the reduction in the kinetics of spherulites growth is

* Corresponding authors.
E-mail addresses: f.hemmati@ut.ac.ir (F. Hemmati), H.Khonakdar@ippi.ac.ir (H.A. Khonakdar).
[1] The contribution of the first and second authors is equal.

https://doi.org/10.1016/j.arabjc.2023.105522
Received 3 October 2023; Accepted 3 December 2023
Available online 5 December 2023

attributed to chain movements, the free energy of nucleation and the competition between the progressive growth rate of the crystal surface and the penetration of amorphous phase chains into the interlayer regions (Luyten et al., 1997).

PCL/SAN blends have lower critical solution temperature (LCST) phase behavior at high temperatures and at lower temperatures, these mixtures show an apparent upper critical solution temperature (UCST) phase diagram below the melting point of PCL. The virtual UCST phase diagram is due to the crystallization process of PCL chains in the presence of amorphous SAN macromolecules (Schulze et al., 1993; Svoboda et al., 1994). LCST phase diagram, spinodal decomposition kinetics, dissolution of phases in each other and PCL phase crystallization in PCL/SAN blends have been studied by many scientists (Salkhi Khasraghi et al., 2022; Su and Lin, 2004; Naziri et al., 2019). Since the isothermal crystallization kinetics of PCL melt in PCL/SAN blends is greatly affected by the presence of amorphous SAN chains, Madbouly et al. investigated the isothermal crystallization process of PCL/SAN (80/20) blend containing 27.5 % by weight of acrylonitrile. The authors found that the half-crystallization time of PCL in the blends changed by annealing at temperatures above the LCST phase diagram. It was found that the crystallization kinetics of PCL in the blend was greatly enhanced by liquid–liquid phase separation (Salkhi Khasraghi et al., 2022).

Polymer blends that exhibit phase separation may not always perform optimally in service, therefore, the development of suitable interfacial additives or compatibilizers has always been one of the major topics in the research of polymer blends (Svoboda et al., 2008). In addition to the positive effects of nanoparticles on the final properties of polymer blends, the introduction of nanoparticles into blends as compatibilizers has been widely reported as well (Madbouly et al., 2006; Azizli et al., 2020; Mdletshe et al., 2015). The final properties and performance of a composite system containing nanofiller depend on the localization and dispersion state of nanofiller (Mdletshe et al., 2015; Crosby and Lee, 2007; Qian et al., 2016; Naziri et al., 2020).

Numerous studies have been dedicated to PCL and its mixtures aimed at increasing the rate of biodegradation and crystallization (Hosseiny et al., 2020; Arshian et al., 2023). Composite membranes of the PCL/chitosan (CS) blends were prepared by applying the lyophilization method by Zhang et al. at different blend ratios (Fakhri et al., 2021). Their findings demonstrated the importance of the blend composition on the morphology and mechanical performance of the membranes. The blend with 10/90 w/w CS/PCL composition had the optimum properties suggested for tissue engineering applications. At this composition, the crystallinity degree and membrane porosity increased by 29.97 % and 85.61 %, respectively (Fakhri et al., 2021). The influences of poly (propylene carbonate) (PPC) on the thermal, mechanical and rheological properties of the PCL/PPC blends were studied by Li et al. in 2022 (Albertsson and Varma, 2002). It was reported, in these immiscible blends, that the presence of PPC phase accelerated the PCL crystallization process and reduced the PCL crystallinity degree. As a result, considerable enhancements in the PCL stiffness, strength and melt elasticity were obtained by the melt-blending of PCL with PPC (Albertsson and Varma, 2002).

In a recently published work, the effects of the PCL and pre-stretch rate (of the extrusion-casting-thermal stretching process) on the mechanical performance and crystallinity of the poly(glycolic acid)/PCL blends have been investigated. Their findings show that high tensile strength and elongation-at-break were achieved at higher molecular orientation and lower crystallinity by applying higher pre-stretching temperature (Zhang et al., 2021). In another research, the effects of PCL presence and content on the properties of the air-jet spun poly(3-hydroxybutyrate-co-3-hydroxyvalerate) (PHBV)/PCL fibrous scaffolds were evaluated. The results confirm the beneficial role of PCL on the crystallinity, thermal stability and mechanical properties of the PCL/PHBV blend scaffolds (Li et al., 2022). Mathematical modeling was applied, in another recently published study, for optimizing the mechanical properties of the melt-blown films of the ternary blends based on poly(lactic acid) (PLA)/PCL/cellulose acetate butyrate (CAB). The improved miscibility of the components caused the attainment of the films with the largest strain at break at the composition of 55–85 wt% PLA, 5–20 wt% PCL and 10–25 wt% CAB (Xu et al., 2023). All of these works clarify the importance of processing, phase miscibility and crystallinity in controlling the blend properties.

Isothermal and non-isothermal crystallization kinetics of pure PCL and its blends have been also reported in the presence of nanoparticles (Madbouly and Ougizawa, 2004; Kalva et al., 2023; Tuancharoensri et al., 2023). Jing Qian et al. investigated the morphology and crystallization behavior of PCL/SAN in a (20/80) blend containing 30 % by weight of AN comonomer in SAN in the presence of hydrophobic and hydrophilic nanosilica. It was found that hydrophilic nanosilica had a significant effect on the morphology of PCL/SAN blend compared to hydrophobic nanosilica. The nucleation ability of hydrophobic nanosilica in PCL showed its limitations because the effect of nanosilica on crystal growth is always greater than its heterogeneous nucleation effect (Mdletshe et al., 2015).

In our previous works, the effects of spherical nanosilica particles on the LCST phase diagram of PCL/SAN blends and the non-isothermal crystallization kinetics of PCL in the blends were studied. In this research, it was observed that the thermodynamic equilibrium LCST phase diagram of PCL/SAN blends unexpectedly shift to lower temperatures by adding hydrophilic nanosilica. The migration of nanosilica particles to SAN-rich regions, especially at lower cooling rates of rheometric tests, has led to unfavorable PCL/SAN enthalpy interactions and much larger dynamic asymmetry of polymer components (Maghoul et al., 2023). In another work, the non-isothermal crystallization of PCL chains in PCL/SAN blends was investigated in the presence of two types of hydrophilic and hydrophobic nanosilica. Hydrophobic silica nanoparticles significantly accelerated the crystallization process of PCL in PCL/SAN (80/20) blend, while the hydrophilic silica nanoparticles contributed only slightly to the PCL crystallization process. The reason for this is the selective migration of hydrophilic silica nanoparticles to the phase-separated regions of SAN during the non-isothermal DSC test (Mohtaramzadeh et al., 2020).

Studying the kinetic phenomenon of the non-isothermal crystallization of PCL in PCL/SAN blends in the presence of nanoparticles is very complicated and challenging. The complexity originates from the presence of the LCST phase diagram of PCL/SAN, selective migration of nanoparticles to one of two phases after phase separation, effects of nanoparticles on phase separation boundary and kinetics of mutual dissolution of two polymers during the test. Although several studies have been conducted on the crystallization of PCL in the PCL/SAN blends in the absence and presence of nanoparticles, the effects of nanoparticles on the LCST phase behavior of PCL/SAN and the migration of nanoparticles during the non-isothermal DSC test have rarely been considered. Therefore, in this research, in continuation of the group's previous works, the crystallization kinetics and crystallization activation energy of PCL in PCL/SAN blends in the presence of hydrophilic and hydrophobic silica nanoparticles are quantitatively studied. In addition to the type of nanoparticles, in this research, the effects of PCL molecular weight on the non-isothermal kinetics of the PCL crystallization and the phenomena that occur during the non-isothermal DSC test are fully investigated. The main objective of this study is getting an insight into the effects of phenomena involved in the cooling process of a filled multi-component system (with LCST phase behavior) as a model system on the crystallization kinetics. The reason for this selection is the similarity of a non-isothermal crystallization of a polymer in the presence of amorphous polymer and nanoparticles with what is done during the cooling process of the industrial production of the multiphase polymeric products.

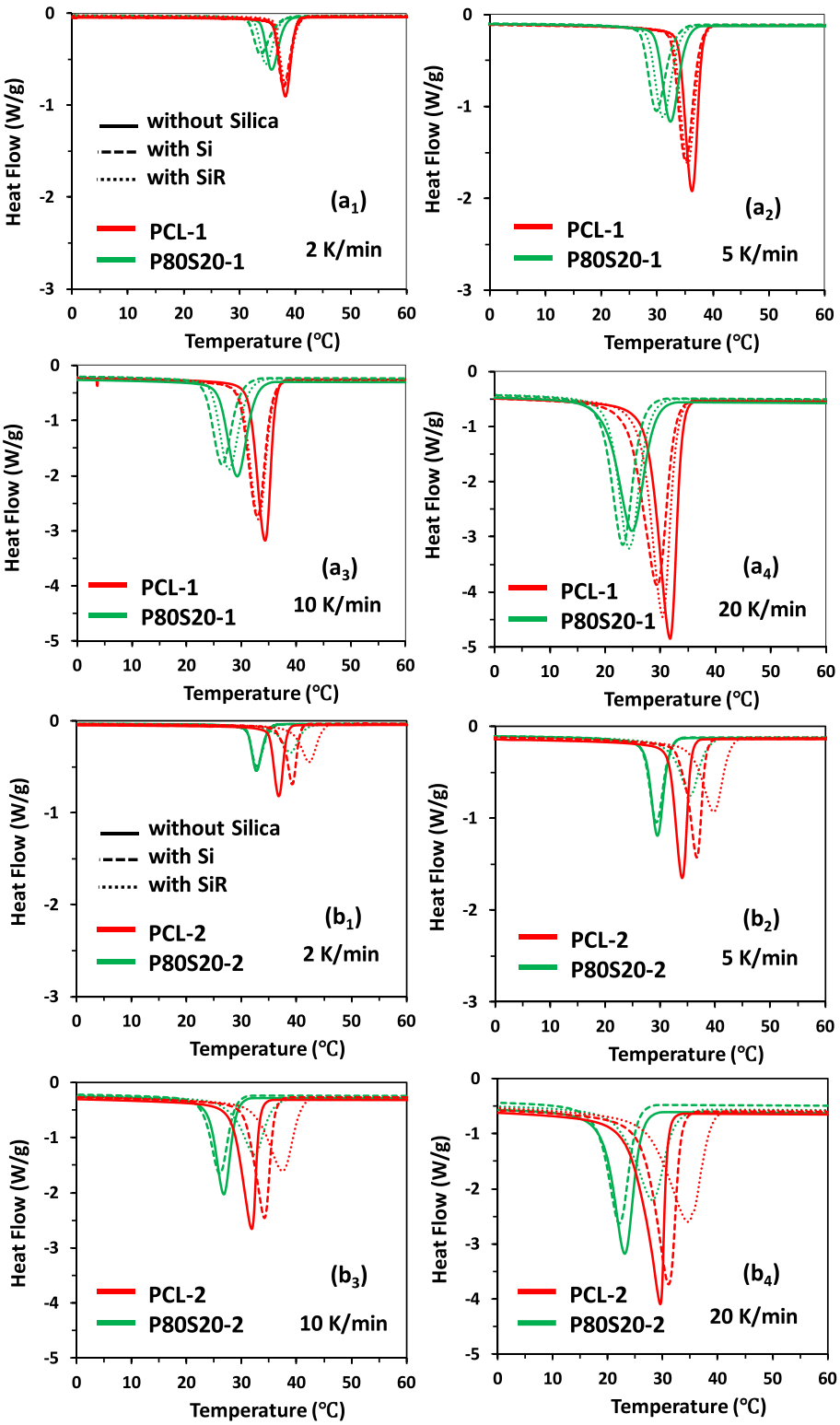

Fig. 1. Heat flow curves for the non-isothermal crystallization of virgin PCL-1, P80S20-1, and their nanocomposites filled with Si and SiR at different cooling rates: (a_1) 2 K/min, (a_2) 5 K/min, (a_3) 10 K/min, and (a_4) 20 K/min, as well as PCL-2 and P80S20-2 and their nanocomposites filled with Si and SiR at different cooling rates: (b_1) 2 K/min, (b_2) 5 K/min, (b_3) 10 K/min, and (b_4) 20 K/min.

2. Experimental

2.1. Materials

Two grades of PCL, the first one 704,105 grade with M_n = 45 kg.mol^{-1} and melting point (T_m) of 56 °C and the second one 440,744 grade with M_n = 80 kg.mol^{-1} and T_m of 60 °C, were purchased from Sigma-Aldrich Co. (Darmstadt, Germany). These two grades were assigned as PCL-1 and PCL-2, respectively. Poly(styrene-co-acrylonitrile) copolymer, SAN, with the grade of 182,850 (M_w = 165 kg mol^{-1} and 25 wt% content of acrylonitrile (AN)) was also supplied from Sigma-Aldrich Co (Darmstadt, Germany). Two grades of fumed silica with a 12 nm primary

Table 1
Data obtained from the fitting of Avrami and Jeziorny models on the non-isothermal crystallization data for all the prepared samples (considering a three-stage crystallization).

Sample	ϕ	n_1	Z_{t1}	Z_{c1}	$\tau_1(1/2)$	n_2	Z_{t2}	Z_{c2}	$\tau_2(1/2)$	n_3	Z_{t3}	Z_{c3}	$\tau_3(1/2)$
PCL-1	2	1.093	1.87E-03	0.043	2.25E + 02	5.152	0.008	0.092	2.354	1.291	0.557	0.746	1.185
	5	0.957	1.47E-03	0.271	6.21E + 02	4.606	0.686	0.927	1.002	1.134	1.834	1.129	0.424
	10	0.901	1.46E-03	0.520	9.35E + 02	4.237	6.266	1.201	0.595	1.202	3.488	1.133	0.261
	20	1.167	4.33E-03	0.762	7.74E + 01	4.221	42.609	1.206	0.377	1.496	6.437	1.098	0.225
PCL-1-3Si	2	1.313	2.90E-03	0.054	6.48E + 01	4.725	0.006	0.080	2.700	1.422	0.414	0.644	1.436
	5	0.858	7.32E-04	0.236	2.94E + 03	4.559	0.228	0.744	1.283	1.577	1.090	1.017	0.750
	10	0.988	1.50E-03	0.522	4.97E + 02	4.510	2.276	1.086	0.768	1.605	2.588	1.100	0.440
	20	0.692	5.24E-04	0.685	3.26E + 04	4.164	15.076	1.145	0.477	1.864	5.374	1.088	0.333
PCL-1-3SiR	2	1.117	1.83E-03	0.043	2.03E + 02	4.938	0.004	0.063	2.838	1.497	0.360	0.600	1.550
	5	0.909	1.05E-03	0.254	1.27E + 03	4.889	0.173	0.704	1.329	1.561	1.077	1.015	0.754
	10	0.686	5.05E-04	0.468	3.74E + 04	4.391	2.549	1.098	0.743	1.447	2.688	1.104	0.392
	20	0.817	8.10E-04	0.701	3.87E + 03	4.045	22.423	1.168	0.423	1.702	6.302	1.096	0.273
P80S20-1	2	0.995	1.48E-03	0.039	4.80E + 02	5.147	0.002	0.041	3.210	1.262	0.390	0.624	1.578
	5	1.107	2.91E-03	0.311	1.40E + 02	5.123	0.058	0.566	1.624	1.339	0.932	0.986	0.802
	10	1.177	4.33E-03	0.580	7.48E + 01	5.045	0.813	0.980	0.969	1.317	1.906	0.980	0.969
	20	1.147	8.15E-03	0.786	4.82E + 01	4.698	8.177	1.111	0.591	1.634	3.999	1.072	0.342
P80S20-1-3Si	2	1.375	2.16E-03	0.047	6.64E + 01	4.841	0.001	0.026	4.176	1.801	0.116	0.341	2.694
	5	1.235	3.38E-03	0.320	7.44E + 01	4.803	0.043	0.534	1.781	1.575	0.683	0.927	1.009
	10	1.254	5.64E-03	0.596	4.64E + 01	4.532	0.814	0.980	0.965	1.489	1.851	1.063	0.517
	20	1.267	1.04E-02	0.796	2.74E + 01	4.311	11.800	1.131	0.518	1.585	4.707	1.081	0.299
P80S20-1-3SiR	2	1.284	3.18E-03	0.056	6.62E + 01	5.026	0.002	0.046	3.178	1.386	0.336	0.580	1.684
	5	1.228	4.35E-03	0.337	6.22E + 01	4.689	0.083	0.608	1.571	1.344	0.936	0.987	0.800
	10	1.119	4.23E-03	0.579	9.54E + 01	4.485	0.968	0.997	0.928	1.216	2.005	1.072	0.417
	20	1.262	8.96E-03	0.790	3.13E + 01	4.468	11.421	1.129	0.534	1.413	4.542	1.079	0.264
PCL-2	2	0.966	2.57E-03	0.051	3.29E + 02	5.409	0.006	0.081	2.372	1.344	0.449	0.670	1.381
	5	0.928	2.83E-03	0.309	3.75E + 02	4.310	0.745	0.943	0.983	1.410	1.482	1.082	0.583
	10	1.285	9.20E-03	0.626	2.89E + 01	4.096	6.044	1.197	0.589	1.467	2.985	1.056	0.370
	20	1.590	3.86E-02	0.850	6.15E + 00	4.054	39.838	1.202	0.368	1.496	5.133	1.085	0.262
PCL-2-3Si	2	1.155	2.23E-03	0.047	1.44E + 02	4.941	0.014	0.117	2.210	1.413	0.389	0.624	1.504
	5	0.968	1.40E-03	0.269	6.07E + 02	4.673	0.472	0.861	1.086	1.571	1.139	1.026	0.729
	10	0.929	9.05E-04	0.496	1.27E + 03	4.360	5.439	1.185	0.623	1.488	2.668	1.050	0.404
	20	1.567	2.42E-02	0.830	8.52E + 00	4.079	28.379	1.182	0.402	1.633	4.962	1.083	0.300
PCL-2-3SiR	2	1.323	2.99E-03	0.055	6.14E + 01	4.544	0.003	0.059	3.204	1.564	0.166	0.408	2.493
	5	0.940	1.58E-03	0.275	6.49E + 02	4.168	0.146	0.680	1.453	1.799	0.517	0.876	1.177
	10	0.770	1.09E-03	0.505	4.38E + 03	4.059	1.406	1.035	0.840	1.852	1.407	1.017	0.682
	20	0.630	5.15E-04	0.685	9.25E + 04	3.919	8.810	1.115	0.523	1.953	3.414	1.063	0.442
P80S20-2	2	1.177	5.26E-03	0.073	6.32E + 01	5.839	0.001	0.027	3.251	1.373	0.312	0.558	1.791
	5	1.075	2.87E-03	0.310	1.65E + 02	5.449	0.124	0.658	1.372	1.465	0.898	0.979	0.838
	10	1.024	2.64E-03	0.552	2.30E + 02	4.587	3.128	1.121	0.720	1.101	2.384	1.091	0.326
	20	1.432	1.59E-02	0.813	1.40E + 01	4.405	20.123	1.162	0.465	1.405	4.193	1.074	0.278
P80S20-2-3Si	2	1.277	3.26E-03	0.057	6.65E + 01	5.370	0.001	0.036	3.223	1.412	0.286	0.535	1.870
	5	1.063	2.14E-03	0.292	2.31E + 02	4.881	0.153	0.687	1.362	1.436	0.935	0.987	0.812
	10	1.180	4.68E-03	0.585	6.92E + 01	4.720	2.268	1.085	0.778	1.362	2.093	1.077	0.444
	20	1.505	1.83E-02	0.819	1.12E + 01	4.245	18.043	1.156	0.464	1.416	4.216	1.075	0.279
P80S20-2-3SiR	2	1.219	4.70E-03	0.069	6.00E + 01	4.596	0.001	0.036	3.911	1.806	0.093	0.305	3.038
	5	1.125	8.24E-03	0.383	5.13E + 01	4.164	0.076	0.597	1.701	1.698	0.436	0.847	1.315
	10	1.657	2.60E-02	0.694	7.25E + 00	4.080	0.732	0.969	0.987	1.715	1.174	1.016	0.736
	20	1.003	5.13E-03	0.768	1.33E + 02	3.911	4.037	1.072	0.637	1.894	2.892	1.055	0.470

particle size, hydrophilic fumed silica (Aerosil® 200 with a 200 m^2/g specific surface area) and hydrophobic fumed silica (Aerosil® R104 with a 150 m^2/g specific surface area), were purchased from Evonik Co. (Essen, Germany). These nanosilica grades were represented as Si (hydrophilic) and SiR (hydrophobic) nanoparticles, respectively.

2.2. Sample preparation

The binary blends of PCL/SAN and the nanosilica-filled systems, with various SAN contents (0, 10, 20, 30, 40, 50, and 100 wt%) and two different molecular weights (M_n) of PCL, were melt-compounded using a micro-compounder, DACA Instruments (Santa Barbara, California) at a rotor speed of 100 rpm and a temperature of 160 °C for 10 min. The nanosilica loadings (Si or SiR) were 3 phr in the PCL/SAN/silica nanocomposites. The components were fed to the compounder simultaneously. All samples were then compression molded using a lab-scale hot press (Davenport 25 tons) to sheets with an average thickness of 1 mm. The fabricated samples are referred to PxSy-z blends as well as PxSy-z-3Si and PxSy-z-3SiR nanocomposites, where x, y, and z represent the PCL (wt%) and SAN (wt%) weight percentages, and the applied PCL grade in the sample, respectively. In the same way, the virgin PCL grades and PCL/silica nanocomposites are represented as PCL-z and PCL-z-3Si or PCL-z-3SiR nanocomposites.

2.3. Characterizations

The effect of silica nanoparticles and the M_n of PCL on the PCL's crystallization behavior in semicrystalline PCL/SAN blends were assessed using differential scanning calorimeter (DSC, TA Instruments (Trios)) through a non-isothermal study. The specimens were first heated from −100 to 130 °C under the nitrogen environment (with a flux of 50 ml/min) at a heating rate of 10 °C/min to erase the thermal history. Then, the samples were cooled at various cooling rates of 2, 5, 10, and 20 °C/min from 130 to −100 °C. The indium and tin standard samples were applied to calibrate the temperature and heat flow. The time of attaining 50 % of final crystallinity (the crystallization half-time ($t_{1/2}$)) was calculated to assess the crystallization kinetics.

The dispersion state of nanoparticles and the bulk of some samples were studied using transmission electron microscope (TEM) applying a Philips CM-30 and field emission scanning electron microscope (FESEM)

using Carl Zeiss Group Ultra Plus (Jena, Germany). The ultramicrotome (Leica Biosystems©, Germany) was applied to cut samples at −180 °C. The samples were then sputtered with platinum at a 3 nm rough thickness and examined.

3. Results and discussion

3.1. Results

In this study, non-isothermal DSC studies were conducted on virgin PCL, PCL/SAN blends, PCL/Silica and PCL/SAN/Silica nanocomposites at cooling rates of 2, 5, 10, and 20 °C/min. The thermograms obtained are depicted in Fig. 1. For all samples, the exothermic crystallization peak shifts to lower temperatures, intensifies and broadens with increasing cooling rate. Furthermore, at a constant cooling rate, by adding the SAN component to PCL as well as the increase of M_n of PCL, the crystallization peak is shifted to a lower temperature, flattened, and the area under the peak decreases. The addition of silica nanoparticles affects the crystallization peak of the samples in different ways depending on the nature of the nanoparticles (hydrophilic or hydrophobic) as well as Mn of PCL. In PCL-1-based nanocomposites and P80S20-1-based nanocomposites, the incorporation of nanoparticles broadens the crystallization peak and shifts it to lower temperatures. The shift of the crystallization peak is more dominant with the incorporation of Si nanoparticle. On the contrary, in PCL-2-based nanocomposites, the incorporation of nanoparticles broadens the crystallization peak and shifts it to higher temperatures. The width of the crystallization peak increases with the addition of SiR nanoparticles and is transferred to higher temperatures. In nanocomposites based on P80S20-2, a trend similar to that of PCL-2 nanocomposites can be seen. However, with the addition of Si to P80S20-2, a slight shift to a lower temperature occurs. Similar to P80S20-1 and P80S20-2 samples, hydrophilic and hydrophobic nanosilica fillers affect the PCL crystallization peak of PCL/SAN blends in other compositions. The DSC thermograms of PCL-1-based PCL/SAN blends and nanocomposites are represented in supporting information in Figure S1.

For a better understanding of non-isothermal crystallization kinetics, various models can be applied, such as the Avrami, Ozawa, Jeziorny, and Mo theories (Dhanvijay et al., 2012; Achla, 2017; Avrami, 1940). These models have been frequently applied for studying the non-isothermal crystallization kinetics of PCL-based blends (Kalva et al., 2023; Ozawa, 1971; Jeziorny, 1978; Choi and Kwak, 2004).

3.1.1. Avrami and Jeziorny models

The Avrami equation is the most frequent model utilized for the isothermal crystallization analysis. Modified Avrami is used to examine the crystallization process in this research, according to the following equations:

$$X(T) = 1 - \exp(-Z_t t^n) \tag{1}$$

$$log[-\ln(1 - X(T))] = logZ_t + nlogt \tag{2}$$

$$\tau_{1/2} = [ln2/Z_t]^{1/n} \tag{3}$$

here n, Z_t, and $\tau_{1/2}$ are respectively the Avrami exponent, the crystallization rate constant, and crystallization half-time. The n value is attributed to the crystal growth dimensions and the nucleation mechanism. Fig. 3 shows $log[-\ln(1-X(T))]$ vs. $logt$ curves for samples. The slope and intercept of curves were used to calculate the values of n and Z_t, respectively. The curves appeared at three stages with different slopes, which were considered as regime I (n_1, Z_{t1}), regime II (n_2, Z_{t2}), and regime III (n_3, Z_{t3})). The Avrami parameters including n, Z_t, and $\tau_{1/2}$ for regime I-III are gathered in Table 1. Regime I and II belong to the primary crystallization of PCL phase, while regime III shows the secondary crystallization stage. As can be seen in Table 1, the n value is nearly constant throughout each regime. A change in n value will indicate a change in the crystallization mechanism. The transition between the primary and secondary crystallization processes is therefore detectable by the n value. It should be mentioned that the values of calculated n, Z_t, and $\tau_{1/2}$ by considering the whole of $log[-\ln(1-X(T))]$ vs. $logt$ curves as a single stage are also assessed and reported in Table 2. All of the theoretically calculated values for the crystallization half-time (Eq. (3)) were quite similar to the corresponding experimental values that were directly calculated from the $X(T)$ vs. time curves.

Table 2
Data obtained from the fitting of overall Avrami and Jeziorny models on the non-isothermal crystallization data for all the prepared samples (considering a one-stage crystallization).

Sample	ϕ	n	Z_t	Z_c	$\tau(1/2)$	R^2
PCL-1	2	3.069	0.029	0.172	2.797	0.932
	5	3.189	0.399	0.832	1.189	0.950
	10	3.222	2.351	1.089	0.685	0.962
	20	3.413	11.798	1.131	0.436	0.973
PCL-1-3Si	2	3.011	0.024	0.157	3.035	0.943
	5	3.244	0.206	0.729	1.454	0.952
	10	3.389	1.178	1.017	0.855	0.956
	20	3.404	6.328	1.097	0.522	0.971
PCL-1-3SiR	2	3.084	0.020	0.141	3.170	0.931
	5	3.314	0.180	0.710	1.502	0.939
	10	3.353	1.267	1.024	0.835	0.958
	20	3.366	9.108	1.117	0.465	0.976
P80S20-1	2	3.023	0.012	0.110	3.810	0.928
	5	3.166	0.099	0.630	1.847	0.929
	10	3.304	0.476	0.928	1.120	0.948
	20	3.328	2.852	1.054	0.654	0.959
P80S20-1-3Si	2	2.973	0.008	0.088	4.529	0.935
	5	3.156	0.083	0.608	1.961	0.939
	10	3.200	0.566	0.945	1.066	0.952
	20	3.322	4.159	1.074	0.583	0.963
P80S20-1-3SiR	2	2.899	0.017	0.129	3.624	0.936
	5	3.029	0.120	0.654	1.785	0.943
	10	3.168	0.567	0.945	1.065	0.955
	20	3.244	3.632	1.067	0.600	0.959
PCL-2	2	2.936	0.029	0.169	2.963	0.925
	5	2.998	0.464	0.858	1.143	0.951
	10	3.106	2.395	1.091	0.671	0.965
	20	3.058	8.470	1.113	0.441	0.971
PCL-2-3Si	2	2.785	0.035	0.187	2.923	0.924
	5	3.215	0.306	0.789	1.290	0.951
	10	3.318	2.002	1.072	0.726	0.959
	20	3.167	7.045	1.103	0.481	0.972
PCL-2-3SiR	2	2.775	0.016	0.127	3.873	0.945
	5	2.967	0.144	0.678	1.700	0.957
	10	3.092	0.798	0.978	0.956	0.960
	20	3.145	3.525	1.065	0.596	0.972
P80S20-2	2	2.889	0.016	0.126	3.697	0.920
	5	3.290	0.157	0.690	1.572	0.910
	10	3.382	1.469	1.039	0.801	0.947
	20	3.145	4.255	1.075	0.562	0.962
P80S20-2-3Si	2	2.904	0.015	0.122	3.755	0.930
	5	3.159	0.152	0.686	1.616	0.942
	10	3.155	0.891	0.989	0.923	0.949
	20	3.088	4.090	1.073	0.563	0.968
P80S20-2-3SiR	2	2.663	0.014	0.117	4.368	0.939
	5	2.716	0.111	0.645	1.961	0.955
	10	2.910	0.499	0.933	1.120	0.967
	20	3.068	2.146	1.039	0.692	0.963

For correction of the Z_t parameter in the Avrami equation to include the non-isothermal conditions, the Jeziorny equation is also used which is illustrated in Eq. (4):

$$\log Z_c = \frac{\log Z_t}{\phi} \tag{4}$$

The Z_c values of samples are reported in Table 1 and Table 2 respectively for a three-stage and one-stage crystallization.

According to Table 1, the n value rapidly increased throughout the early phases of the main process over stage 1 to stage 2. The Avrami

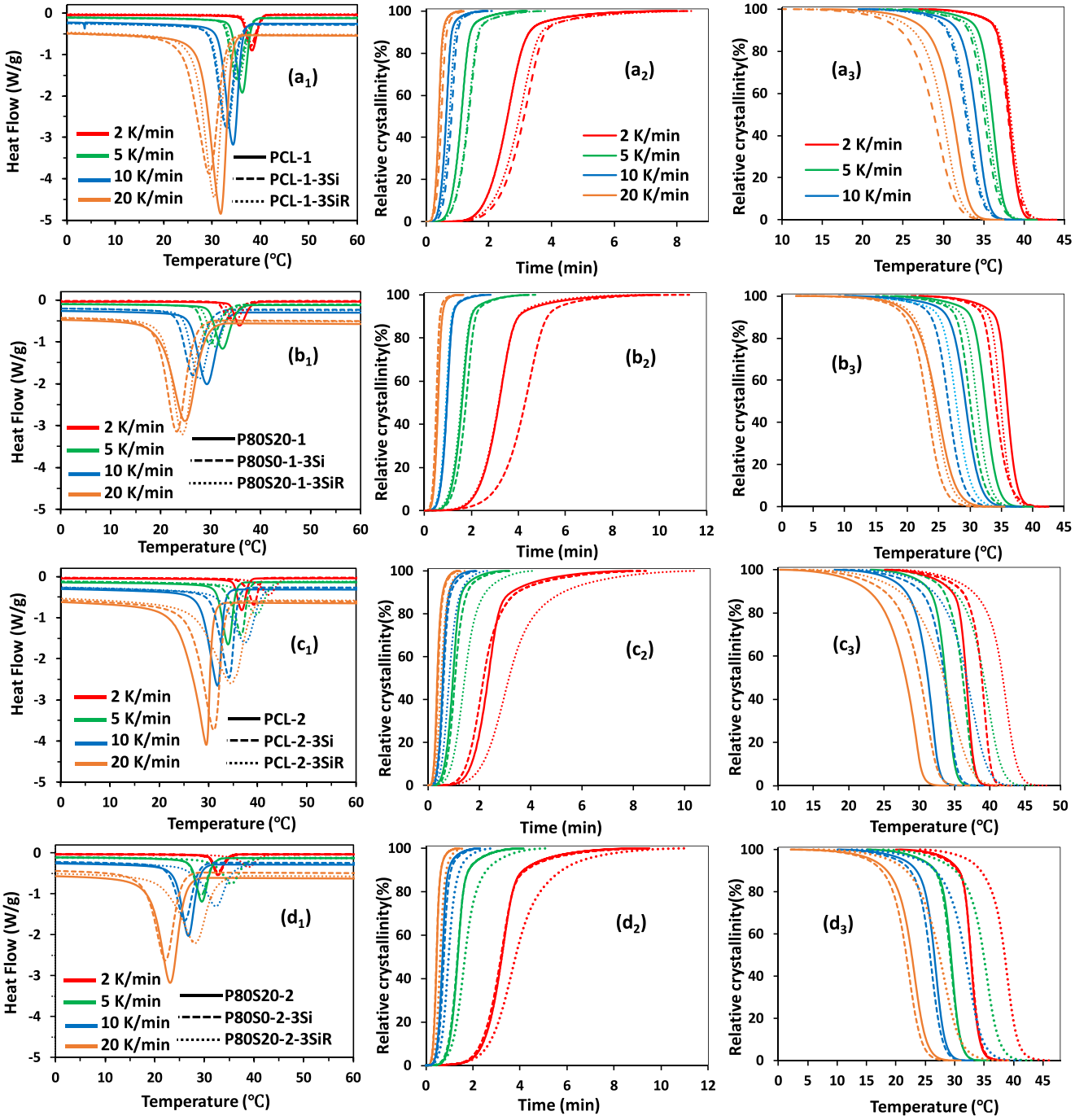

Fig. 2. Heat flow curves and relative degree of crystallinity, X(T), versus time and temperature at different cooling rates for the non-isothermal crystallization of (a_1, a_2, a_3) virgin PCL-1, PCL-1-3Si, and PCL-1-3SiR, (b_1, b_2, b_3) P80S20-1, P80S20-1-3Si, and P80S20-1-3SiR, (c_1, c_2, c_3) virgin PCL-2, PCL-2-3Si, and PCL-2-3SiR, (d_1, d_2, d_3) P80S20-2, P80S20-2-3Si, and P80S20-2-3SiR.

exponent of samples, in the first stage, n_1, and third stage, n_3, respectively is mostly close to 1 and in the range between 1 and 2. However, the second stage's Avrami exponent, n_2, is between 3.92 and 5.53 range, indicating three-dimensional (3D) crystallite growth, as well as heterogeneous and athermal nucleation, for the primary crystallization stage. There was a reduction in n_2 values by increasing the cooling rate, while the values of Z_t and Z_c increased. As well from Table 1, the incorporation of Si and SiR nanoparticles roughly leads to a reduction of n_2 as well as n (Avrami exponent of single-stage crystallization) compared to PCL and PCL80/SAN20 blend samples. P80S20 blends show a higher value of n_2 compared to PCL. However, increasing the molecular weight of PCL mostly leads to a decrease in n values.

Additionally, Z_{t2} and Z_t (crystallization rate constant of single-stage crystallization) and consequently $\tau_{1/2}$ change differently with the incorporation of Si and SiR nanoparticles in pure PCL and P80S20 blends. With the incorporation of Si and SiR nanoparticles into PCL-1 and PCL-2, there was a reduction in Z_{t2} and Z_t values and an increment of $\tau_{1/2}$ at whole cooling rates, only there was an increase of Z_t and a decrease of $\tau_{1/2}$ in PCL-2-3Si compared to PCL-2 at just one cooling rate of 2 K/min. A reduction in Z_{t2} and Z_t values means a decrease in the overall rate of bulk crystallization, in other words overall a slower crystallization rate, by the addition of nanoparticles to pure PCL samples. Indeed, the heat flow curves for non-isothermal crystallization of

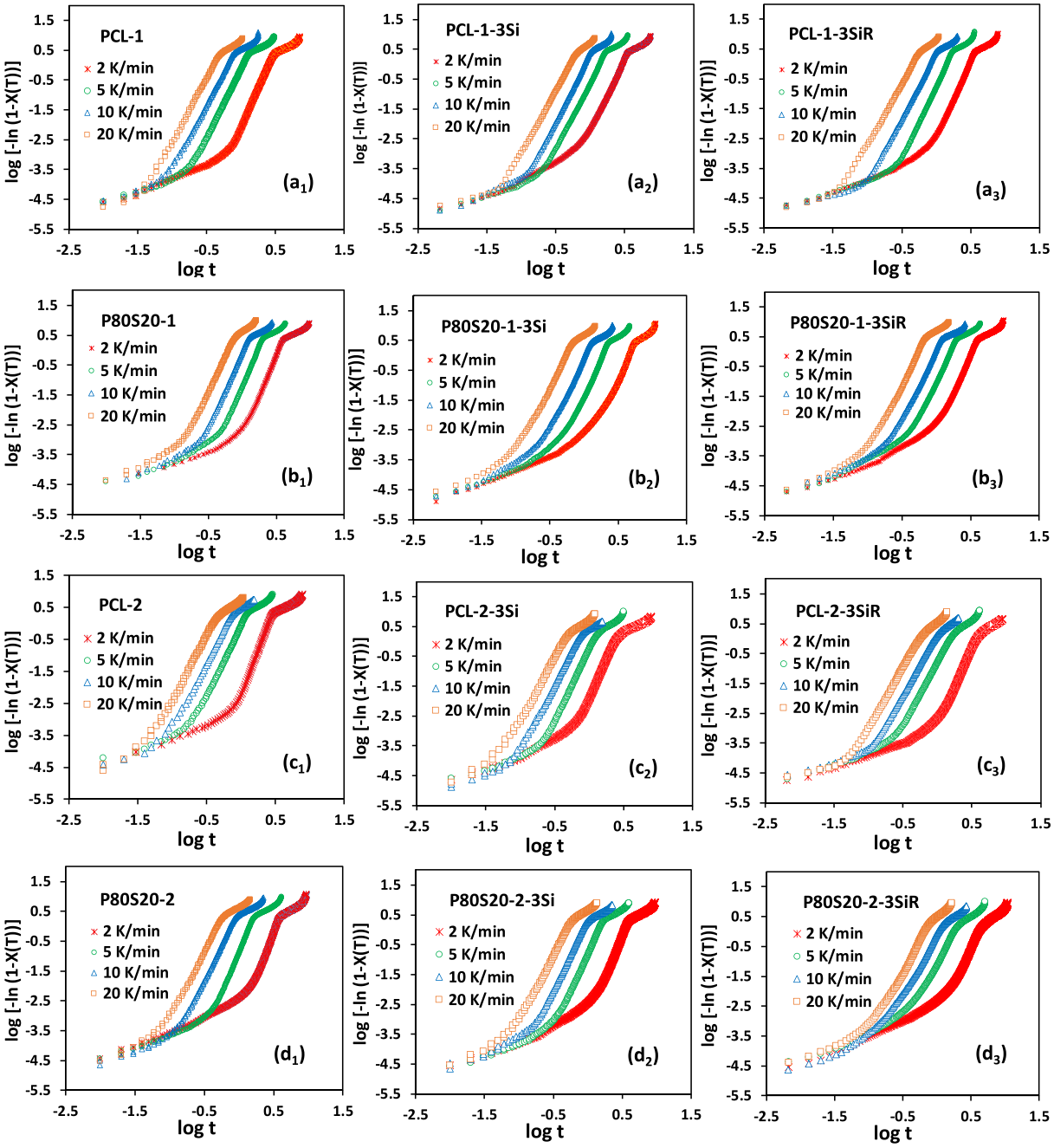

Fig. 3. Plots of Log [-ln(1 - X(T))] versus Log (t) used in the Avrami method for (a_1, a_2, a_3) virgin PCL-1, PCL-1-3Si, and PCL-1-3SiR, (b_1, b_2, b_3) P80S20-1, P80S20-1-3Si, and P80S20-1-3SiR, (c_1, c_2, c_3) virgin PCL-2, PCL-2-3Si, and PCL-2-3SiR, (d_1, d_2, d_3) P80S20-2, P80S20-2-3Si, and P80S20-2-3SiR at different cooling rates.

PCL samples become broader and less sharp through the incorporation of nanoparticles.

In the P80S20-1 blends, the addition of Si leads to a reduction in Z_{t2} at two lower cooling rates (2 and 5 K/min) and an increment of Z_{t2} at two higher cooling rates (10 and 20 K/min). While in all cooling rates with the addition of SiR, an increase in Z_{t2} was obtained. Interestingly, P80S20-2 blends render an adverse trend. The incorporation of Si increases Z_{t2} at two lower cooling rates (2 and 5 K/min), while decreasing it at higher cooling rates. Besides, the incorporation of SiR decreases the Z_{t2} of P80S20-2 roughly in all studied cooling rates. The reduction of Z_{t2} values observed in pure PCL samples due to the addition of nanoparticles indicates the negative effect of nanoparticles on the crystallization kinetics of PCL. However, the reducing effect of SiR incorporation on Z_{t2} in PCL is more pronounced compared to Si, especialy at higher cooling rates.

Crystallization of the samples starts at lower temperatures through the increment of M_n of PCL, as well as the addition of SAN in the P8S20 blends (see third column of Fig. 2). Interestingly, the incorporation of Si and SiR nanoparticles affects the start temperature of crystallization of samples in a different trend. In PCL-1 and P80S20-1-based nanocomposite, the start temperature shifts to the lower temperature in the presence of both hydrophilic and hydrophobic silicas. Although, in the higher M_n PCL-2-based nanocomposites, the start temperature moves to higher temperatures.

Our recent research shows that the increase of SAN concentration in the PCL/SAN blends slows the chain crystallization of PCL and results in significantly lower Z_t and higher $\tau_{1/2}$ (Mohtaramzadeh et al., 2020). This observation is related to a diluting effect of the SAN component on the

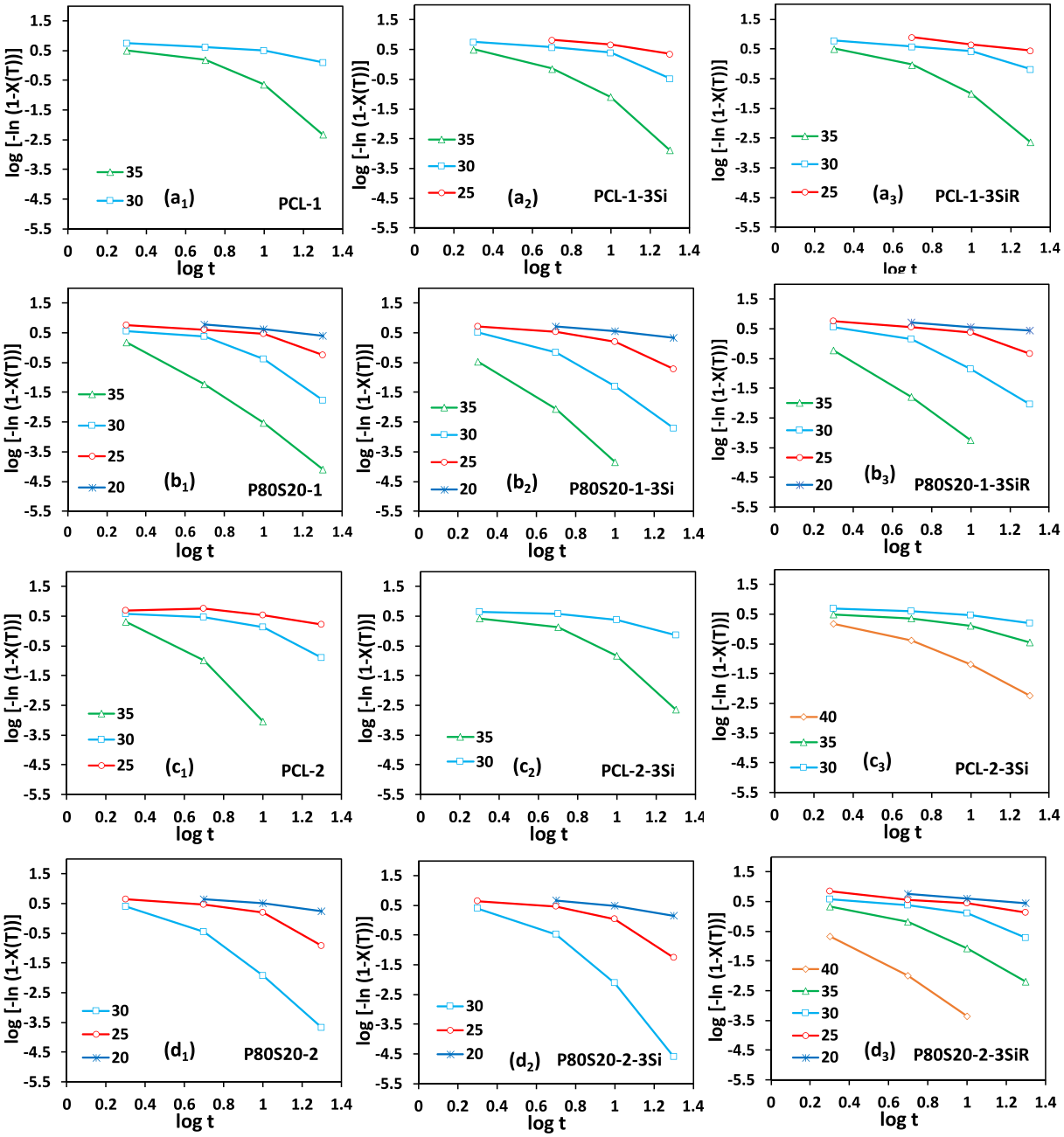

Fig. 4. Ozawa analysis of the non-isothermal crystallization data for Plots of log(ϕ) versus log(t) for the non-isothermal crystallization of (a_1, a_2, a_3) virgin PCL-1, PCL-1-3Si, and PCL-1-3SiR, (b_1, b_2, b_3) P80S20-1, P80S20-1-3Si, and P80S20-1-3SiR, (c_1, c_2, c_3) virgin PCL-2, PCL-2-3Si, and PCL-2-3SiR, (d_1, d_2, d_3) P80S20-2, P80S20-2-3Si, and P80S20-2-3SiR.

crystallization of PCL. In agreement with our previous finding, according to Tables 1 and 2, the P80S20 blends present lower Z_t compared to PCL samples. In addition, the Z_{t2} decreases by increasing the M_n of PCL, as well as incorporating SAN into the P8S20 blends.

A notable feature of Table 1 is that the hydrophobic SiR in virgin PCL and P80S20 samples affects Z_{t2} and $\tau_{1/2}$ more considerably in comparison with hydrophilic Si nanoparticle. In other words, SiR decreases Z_{t2} more profoundly compared to Si and a slower crystallization rate is attained in SiR-filled nanocomposite. Although, in some of the samples such as P80S20-1, the addition of SiR accelerates the crystallization of PCL. Also, the presence of SiR has comparatively more profound impact on the higher M_n-based PCL-2 and P80S20-2 crystallization kinetics. The adverse changes in the PCL crystallization kinetics of P80S20-1 compared to P80S20-2 with the incorporation of SiR could be concluded.

3.1.2. *Ozawa model*

The Ozawa model derived from the Avrami theory is commonly used to explain the dynamics of the non-isothermal crystallization of polymers. The substitution of the cooling rate, ϕ, for the time variable, t, is the fundamental modification applied to the Avrami model in the Ozawa extension. In the Ozawa model, by the assumption of a constant cooling rate for the molten polymer, the Avrami equation is modified to deal with non-isothermal behavior (Achla, 2017). The Eqs. (5) and (6) are applied to calculate the crystallinity degree, $X(T)$, at a constant temperature of T according to Ozawa model, as follows:

Table 3
The values of $K(T)$, the cooling crystallization function, and the Ozawa exponent (m), determined by the Ozawa equation.

Sample	T(°C)	m	$K(T)$	R^2	Sample	T(°C)	M	$K(T)$	R^2
PCL-1	40				PCL-2	40			
	35	2.729	49.24	0.862		35	4.721	82.41	0.957
	30	0.633	10.37	0.876		30	1.399	16.77	0.792
	25					25	0.472	8.77	0.717
	20					20			
PCL-1-3Si	40				PCL-2-3Si	40			
	35	3.3226	68.55	0.916		35	2.998	55.82	0.857
	30	1.1442	18.37	0.806		30	0.745	9.55	0.820
	25	0.8098	26.58	0.973		25			
	20					20			
PCL-1-3Si	40				PCL-2-3SiR	40	2.406	11.75	0.960
	35	3.070	55.32	0.914		35	0.894	7.25	0.871
	30	0.830	11.50	0.827		30	0.485	7.69	0.921
	25	0.546	14.52	0.967		25			
	20					20			
P80S20-1	40				P80S20-2	40			
	35	4.233	18.09	0.992		35			
	30	2.289	38.62	0.849		30	4.087	92.00	0.953
	25	0.920	14.17	0.800		25	1.461	19.77	0.789
	20	0.639	17.20	0.994		20	0.686	14.27	0.953
P80S20-1-3Si	40				P80S20-2-3Si	40			
	35	4.797	11.80	0.987		35			
	30	3.224	56.30	0.953		30	4.944	237.85	0.924
	25	1.386	20.99	0.849		25	1.794	27.73	0.802
	20	0.626	14.42	0.982		20	0.869	19.80	0.962
P80S20-1-3SiR	40				P80S20-2-3SiR	40	3.806	3.34	0.991
	35	4.317	16.90	0.996		35	2.509	19.59	0.946
	30	2.604	39.83	0.930		30	1.240	12.72	0.852
	25	1.033	15.26	0.851		25	0.682	11.40	0.976
	20	0.466	10.97	0.996		20	0.523	13.22	1.000

$$1 - X(T) = exp\left[\frac{-K(T)}{\phi^m}\right] \tag{5}$$

$$log[-\ln(1 - X(T))] = logK(T) - mlog\phi \tag{6}$$

where m is the Ozawa exponent, which is affected from the crystal growth dimensions, and $K(T)$ is the cooling crystallization function (kinetic parameters), which is related to the overall crystallization rate. Indeed, $K(T)$ is considered a sign of the crystallization rate (Goodarzi et al., 2009). The curves obtained from the Ozawa method, $log[1 - X(T)]$ vs. $log\ \phi$, during the crystallization process at various temperatures between 5 and 40 °C are represented in Fig. 4. The slope and intercept of Ozawa curves were used to assess $K(T)$ and m using Eq. (6), which are listed in Table 3. The R-squared (R^2) values for the linear regression of experimental data are also reported in Table 3. It should be kept in mind that the lack of fit of the appropriate model to the experimental data is the reason for omitting the parameter values for different percentages of crystallinity in Table 3. Furthermore, while the Z_t and Z_c parameters exhibit a consistent trend, the $K(T)$ parameter does not display a clear pattern against variables when examining the data. This is due to the model's inadequacy (according to R-squared values) in describing the non-thermal crystallization process.

3.1.3. Mo model

The other theory for studying the non-isothermal crystallization of polymers is the modified approach proposed by Mo et al. This approach results from a combination of the Avrami and Ozawa equations. Accordingly, the crystallinity degree in this theory is related to the cooling rate (ϕ) and the crystallization time (t) or temperature (T_C) (Choolaei et al., 2017). The ϕ is related to the t through Eq. (7) at a specific degree of crystallinity, as follows:

$$log\phi = \log F(T_C) - \alpha log t \tag{7}$$

where $F(T_C) = \left(\frac{K(T)}{Z_t}\right)^{\frac{1}{m}}$ points to the required cooling rate to achieve a specific degree of crystallinity at time t. According to Mo model, the lower values of $F(T_C)$ are referred to the increased crystallization rate (Limwanich et al., 2016; Asadinezhad et al., 2014). In addition, the ratio of the Ozawa parameter (m) to the Avrami exponent (n) is defined as α parameter (Asadinezhad et al., 2014). The slope and intercept of the linear plot of $log\phi$ versus $logt$ is used to calculate α and $F(T_C)$; according to Eq. (7). The linear plots of Mo models for different samples are depicted in Fig. 5 and the resulting data for $F(T_C)$, α, and min R^2 values for each sample are listed on Table 4.

According to plots in Fig. 5, a good agreement between the Mo analysis and experimental data can be concluded. The R^2 values higher than 0.98 result from fitting the Mo model to the data for all samples. Furthermore, there is an increase in the value of $F(T_C)$ by the increasing relative crystallinity, which refers to the attainment of higher crystallinity degrees at higher ϕ at a constant time, t. Almost constant values for α, independent of $X(T)$, are reported (Choolaei et al., 2017). In addition, the α values presented in Table 4 alter very little with the increase of $X(T)$. A reduced $F(T_C)$ value was expected through the acceleration of the crystallization process (Jana and Cho, 2010).

A higher $F(T_C)$ value is resulted for PCL-1 compared to those of PCL-2 samples in all measured $X(T)$, demonstrating that the higher molecular weight PCL-2 can crystallize at a faster rate, which is in line with the result of modified Avrami. In addition, $F(T_C)$ increased with the incorporation of amorphous SAN in the P80S20 blends, which is consistent with modified Avrami and points to slower non-isothermal crystallization kinetics of PCL in P80S20 blends with SAN incorporation.

According to Table 4, Si and SiR incorporation occurred in different trends for different samples.

For virgin PCL-1 and PCL-2 samples, the incorporation of Si and SiR resulted in an increment in $F(T_C)$ at whole $X(T)$, only there was a decrease in $F(T_C)$ for PCL-2-3Si compared to PCL-2 at 20 % $X(T)$. Interestingly, in PCL-1, the incorporation of Si led to a higher increment of $F(T_C)$ in all measured $X(T)$, while the addition of SiR increased $F(T_C)$ more dominantly in PCL-2. This means that Si reduces the crystallization rate more than SiR in PCL-1, while the trend is opposite in higher molecular weight PCL-2 and the incorporation of SiR further decreases the crystallization rate.

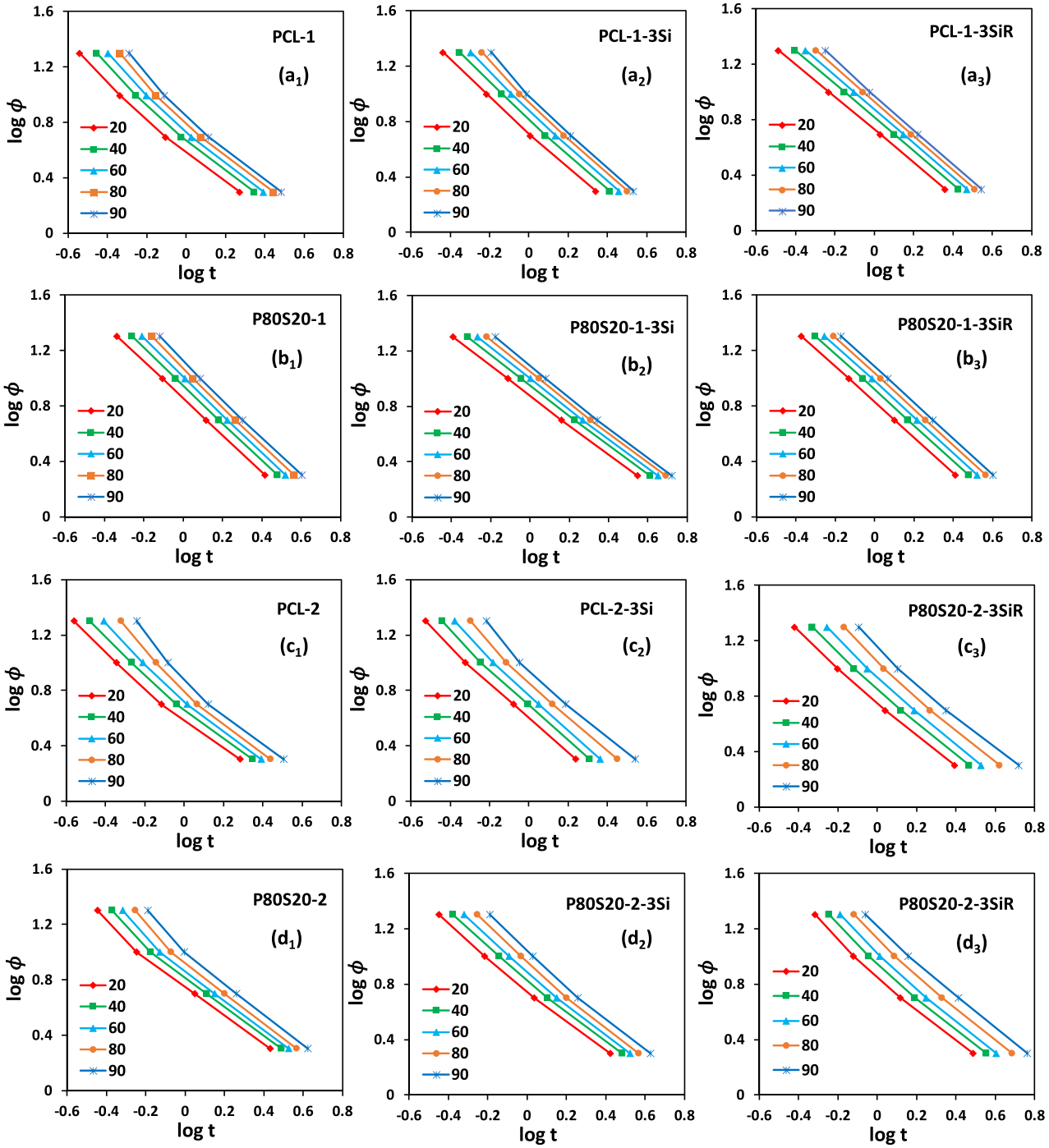

Fig. 5. Plots of log(ϕ) versus log(t) for the non-isothermal crystallization of (a_1, a_2, a_3) virgin PCL-1, PCL-1-3Si, and PCL-1-3SiR, (b_1, b_2, b_3) P80S20-1, P80S20-1-3Si, and P80S20-1-3SiR, (c_1, c_2, c_3) virgin PCL-2, PCL-2-3Si, and PCL-2-3SiR, (d_1, d_2, d_3) P80S20-2, P80S20-2-3Si, and P80S20-2-3SiR.

In P80S20-1, the addition of Si increases $F(T_C)$ at $X(T)$ of 20 % and 40 %, while decreasing $F(T_C)$ at higher $X(T)$. However, the addition of SiR to P80S20-1 decreases the $F(T_C)$ at all $X(T)$ s. In P80S20-2, the incorporation of both Si and SiR results in an increment in $F(T_C)$ at whole $X(T)$ s, only there was a decrease in $F(T_C)$ for P80S20-2-3Si compared to PCL-2 at $X(T)$ of 20 %. The data resulting from the Mo model, which is in agreement with the Avrami model, indicates that the incorporation of Si and SiR to P80S20-1 increases the rate of crystallization, especially at higher $X(T)$ s. In contrast, it demonstrates that the incorporation of Si and SiR into P80S20-2 decreases the rate of crystallization. $F(T_C)$ of P80S20-1 and P80s20-2 is considerably influenced by the incorporation of SiR compared to Si. Indeed, hydrophobic SiR affects the PCL crystallization process more effectively in the P80S20 blend.

3.1.4. *Activation energy of non-isothermal crystallization kinetics*

3.1.4.1. Kissinger method. Kissinger method is applied to assess the activation energy of crystallization (E_C) (Ebadi-Dehaghani et al., 2015; Kissinger, 1956) considering the crystallization peak temperature (T_P) at a constant cooling rate of ϕ as below according to Eq. (8), where R is the universal gas constant.

Table 4
Values of α and $F(T_C)$ parameters against the crystallinity degree based on Mo modification for virgin PCL and P8S20 blends and nanocomposites filled with Si and SiR.

Sample	$X(T)$	α	$F(T_C)$	Min R^2	Sample	$X(T)$	α	$F(T_C)$	Min R^2
PCL-1	20	1.219	4.111	0.990	PCL-2	20	1.180	4.056	0.981
	40	1.240	5.036			40	1.203	4.929	
	60	1.254	5.859			60	1.240	5.731	
	80	1.265	6.783			80	1.302	6.883	
	90	1.274	7.702			90	1.316	8.433	
PCL-1-3Si	20	1.287	5.327	0.996	PCL-2-3Si	20	1.298	4.023	0.990
	40	1.307	6.702			40	1.323	5.004	
	60	1.320	7.800			60	1.339	5.99	
	80	1.344	9.049			80	1.321	7.57	
	90	1.366	10.198			90	1.299	9.486	
PCL-1-3SiR	20	1.178	5.327	0.999	PCL-2-3SiR	20	1.224	5.849	0.995
	40	1.205	6.548			40	1.25	7.439	
	60	1.217	7.489			60	1.267	9.055	
	80	1.235	8.543			80	1.256	11.585	
	90	1.259	9.543			90	1.216	14.282	
P80S20-1	20	1.332	7.19	0.999	P80S20-2	20	1.115	5.861	0.992
	40	1.355	8.88			40	1.14	6.941	
	60	1.372	10.309			60	1.161	7.827	
	80	1.384	11.899			80	1.194	9.087	
	90	1.386	13.452			90	1.207	10.892	
P80S20-1-3Si	20	1.069	7.586	0.999	P80S20-2-3Si	20	1.146	5.851	0.996
	40	1.079	8.98			40	1.163	6.987	
	60	1.089	10.065			60	1.186	7.998	
	80	1.101	11.272			80	1.219	9.391	
	90	1.115	12.405			90	1.22	11.161	
P80S20-1-3SiR	20	1.277	6.733	0.982	P80S20-2-3SiR	20	1.231	7.554	0.994
	40	1.288	8.264			40	1.243	9.29	
	60	1.293	9.484			60	1.249	10.929	
	80	1.296	10.842			80	1.234	13.477	
	90	1.295	12.109			90	1.209	16.252	

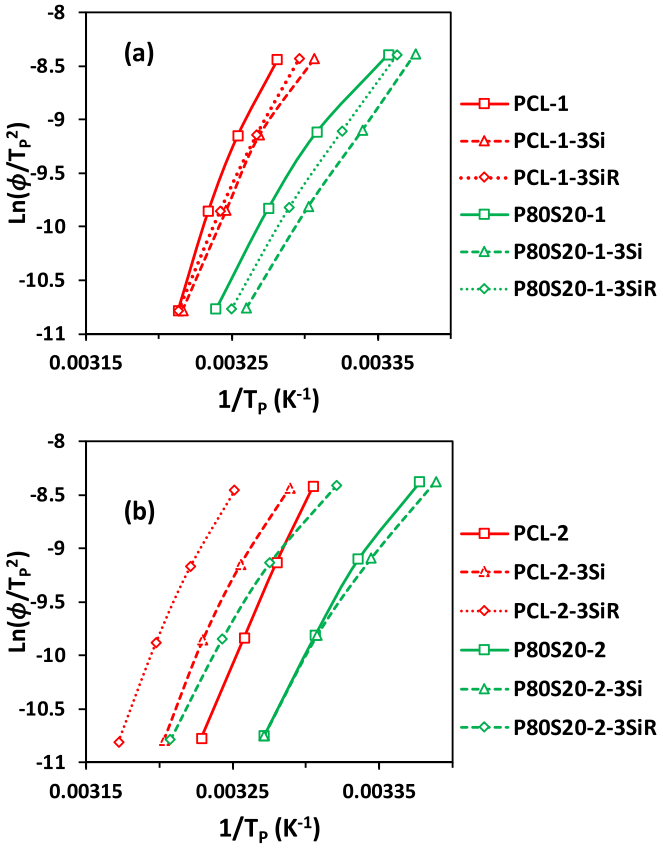

Fig. 6. Kissinger plots for (a) virgin PCL-1, PCL-1-3Si, PCL-1-3SiR, P80S20-1, P80S20-1-3Si, and P80S20-1-3SiR, (b) virgin PCL-2, PCL-2-3Si, PCL-2-3SiR, P80S20-2, P80S20-2-3Si, and P80S20-2-3SiR.

Table 5
The activation energy of PCL crystallization for virgin PCL and P80S20 blends and their nanocomposites filled with Si and SiR.

Sample	$E_C = (kJ.mol^{-1})$	Sample	$E_C = (kJ.mol^{-1})$
PCL-1	285.21	PCL-2	256.97
PCL-1-3Si	235.91	PCL-2-3Si	226.66
PCL-1-3SiR	218.00	PCL-2-3SiR	247.39
P80S20-1	165.91	P80S20-2	186.05
P80S20-1-3Si	172.96	P80S20-2-3Si	167.18
P80S20-1-3SiR	169.89	P80S20-2-3SiR	173.53

$$\frac{d(ln[\phi/T_P^2])}{d(1/T_P)} = -\frac{E_C}{R} \tag{8}$$

The plots of $ln[\phi/T_P^2]$ vs. $1/T_P$ for all samples were depicted in Fig. 6, which shows a good linear relation. The slopes of Kissinger plots is used to calculate the E_C, which are given in Table 5.

E_C is considered an activation energy needed to make motion of the macromolecular segments toward the growing surface of crystalline lamellae. The smaller values for E_C lead to easier crystallization of polymer chains (Su and Lin, 2004). As expected, the higher the molecular weight PCL, the lower the E_C. The activation energy of crystallization is gradually reduced by the growth of the M_n of polymers. The incorporation of the SAN components in P80S20 blends reduces the activation energy of PCL crystallization, relating to the hindrance of amorphous SAN on the PCL crystallization process, which is in agreement with the Avrami and Jeziorny results. An interesting point of Table 5 is that the P80S20-1 has a lower E_C compared to P80S20-2. In other words, the presence of SAN facilities the crystallization of PCL in P80S20-1 more compared to P80S20-2.

E_C is decreased by adding 3 wt% of both Si and SiR to PCL-1 and PCL-2. The reduction of E_C by the incorporation of nanofiller is more obvious in lower molecular weight PCL-1 (17 % reduction for the addition of Si and 24 % reduction for SiR). Indeed, a very small change is observed by the addition of nanosilica to PCL-2 (12 % reduction for the addition of Si

Table 6
The T_P and degree of crystallization (χ_c) of PCL/silica and P80S20/silica nanocomposites at different cooling rates.

Sample	χ_c(%)				T_P(°C)			
	ϕ(°C/min)							
	2	5	10	20	2	5	10	20
PCL-1	46.88	43.73	41.94	39.93	38.24	36.25	34.35	31.8
PCL-1-3Si	46.42	44.37	43.20	41.70	37.94	35.08	32.92	29.45
PCL-1-3SiR	44.49	44.63	43.29	40.09	38.24	35.48	33.12	30.41
P80S20-1	45.62	42.82	41.77	39.25	35.75	32.37	29.29	24.87
P80S20-1-3Si	43.42	42.39	39.70	38.10	33.76	29.84	26.47	23.26
P80S20-1-3SiR	43.97	43.13	41.90	38.55	34.72	31.05	27.74	24.34
PCL-2	38.26	36.12	34.81	34.75	36.75	33.98	31.9	29.6
PCL-2-3Si	38.16	36.18	35.88	35.49	39.21	36.64	34.18	31.06
PCL-2-3SiR	38.43	36.22	35.35	35.33	42.26	39.73	37.48	34.61
P80S20-2	36.14	36.13	34.82	34.68	32.69	29.48	26.81	23.11
P80S20-2-3Si	36.90	35.02	33.35	31.09	32.7	29.34	26.02	22.14
P80S20-2-3SiR	37.09	36.08	34.24	33.37	38.79	35.39	32.32	28.16

and 4 % reduction for SiR). The presence of SiR reduces the E_C of PCL-1 more considerably than Si. While the reverse effect has been observed by the incorporation of nanofiller into PCL-2, Si leads to a higher reduction of E_C in PCL-2. The lower E_C of silica-filled PCL-1 and PCL-2 compared to neat PCL-1 and PCL-2, considering the improved degree of crystallinity of both neat PCL in the presense of Si and SiR, indicates a positive effect of nanosilica on the PCL crystallization process. However, the presence of hyrophobic SiR in PCL-1 facilitates the crystallization more effectively.

Intriguingly, the increment of E_C is resulted by the incorporation of both Si (4.2 %) and SiR (2.4 %) to P80S20-1. While the addition of both Si (11 %) and SiR (6.7 %) reduces the E_C of nanocomposites compared to P80S20-2. The data of the Kissinger model are in agreement with the results of the Avrami and Jeziorny equations.

Considering the variation of T_P at different cooling rates (see Table 6) will also shed light on the effect of nanosilica on the crystallization of PCL. According to Table 6, by increasing the M_n of PCL, as well as incorporating SAN into the P8S20 blends, T_P shifts to lower temperatures. Interestingly, T_P is affected differently by the addition of Si and SiR nanoparticles to the pure PCL and P80S20 blends depending on the M_n of PCL in the sample formulations. Incorporation of Si and SiR nanoparticles into a lower M_n PCL-1 and P80S20-1 leads to a shift in T_P to lower temperatures, while in higher M_n PCL-2 and P80S20-2, T_P shifts to higher temperatures. Only in the P80S20-2 sample, adding 3 wt% hydrophilic silica did not cause any noticeable changes in T_P.

Table 6, also lists the values of the calculated degree of crystallinity (χ_c) of the samples according to Eq. (9), as follows:

$$\chi_c = \frac{\Delta H_C}{\Delta H_C^0 \times W_{PCL}} \times 100 \tag{9}$$

where ΔH_C is the crystallization enthalpy measured based on the area under the crystallization peak, ΔH_C^0 is the specific fusion enthalpy of 100 % crystalline PCL with the value of 139.5 J/g (Madbouly, 2011), and W_{PCL} is the PCL weight fraction in samples, which is considered as 1 in pure PCL samples, 0.97 in PCL/Silica nanocomposites, 0.8 in P80S20 blends, and 0.78 in P80S20/Silica nanocomposites.

The addition of both Si and SiR led to an increment in the crystallinity of PCL in both PCL-1 and PCL-2-based nanocomposites, especially at higher cooling rates, which can be related to the nucleation effect of nanoparticles. The nucleation effect of nanoparticles leads to a reduction in E_C. In the case of P80S20-based nanocomposites, mainly a slight decrease in crystallinity is estimated compared to P80S20 blends. This reduction is more considerable in Si-filled samples compared to SiR-filled samples.

According to Table 6, there is a decrease in χ_c by increasing the M_n of PCL, as well as incorporating SAN in the P80S20 blends. Although the incorporation of Si and SiR nanoparticles into pure PCL samples slows down the crystallization rate (Z_t) of PCL, it leads to an increment in χ_c, especially at higher cooling rates. This means the nucleation effect of nanoparticles in PCL/Silica nanocomposites.

3.1.4.2. Friedman method. The Friedman approach (Jafari et al., 2019; Friedman, 1964) is another model used for a non-isothermal study based on the assessment of the effective energy barrier for crystallization according to the Eq. (10),

$$\ln\left(\frac{dx}{dt}\right) = constant - \frac{\Delta E_C}{RT_{x,i}} \tag{10}$$

where ΔE_C is the effective activation energy, $T_{x,i}$ is the crystallization temperature in a determined $X_C(T)$ at a specific cooling rate, ϕ, and $\frac{dx}{dt}$ is the instantaneous crystallization rate as a function of time at a given conversion, x. Indeed, at a preset $X_C(T)$ at $T_{x,i}$ (Asadinezhad et al., 2014); $\frac{dx}{dt}$ values can be provided by choosing the appropriate crystallinity degree (for example from 10 to 90 %). By plotting $\ln(\frac{dx}{dt})$ against $\frac{1}{T_{x,i}}$, as displayed in Fig. 7, a linear line with the slope of $\frac{\Delta E_C}{R}$ is obtained. The resulting effective activation energies of samples are also provided in Table 7.

The results from Table 7 show that, in general, there is a decreasing trend for ΔE_C with an increase of $X_C(T)$ for most of the samples. The addition of SAN to PCL-1 in P80S20-1 reduces ΔE_C, which is in agreement with the Kissinger technique. As well, it is consistent with the findings of Avrami, Jeziorny, and Mo equations. While the increment of ΔE_C is resulted by the addition of SAN to PCL-2 in P80S20-2. The observed trend for P80S20 blends indicates the ease of PCL crystallization process for PCL-1, while its hardening for PCL-2 in the presence of amorphous SAN. This was also confirmed in our latest research, whereas the higher effective activation energy resulted in P90S10-2 and P80S20-2 compared to PCL-2. Although it should be considered that the crystallinity of PCL in the P80S20 blend compared to pure PCL is reduced in P80S20-1, but in P80S20-2 it is almost the same.

ΔE_C reduces by adding both Si and SiR to pure PCL-1, while it increases by the addition of both nanosilica in the case of P80S20-1. This data is similar to the trend observed in the Kissinger technique and in agreement with the results of the Avrami, Jeziorny, and Mo equations. Indeed, the incorporation of Si and SiR accelerates the crystallization kinetics of PCL, while it slows it down for P80S20-1. SiR affects the trend more considerably at lower crystallinity degrees, while the effect of Si is more dominant at higher crystallinity degrees.

The contradictory data from those of the Kissinger model is the increment of ΔE_C in PCL-2 by incorporation of Si and SiR, although the reduction of E_C of PCL-2 in the Kissinger model in the presence of

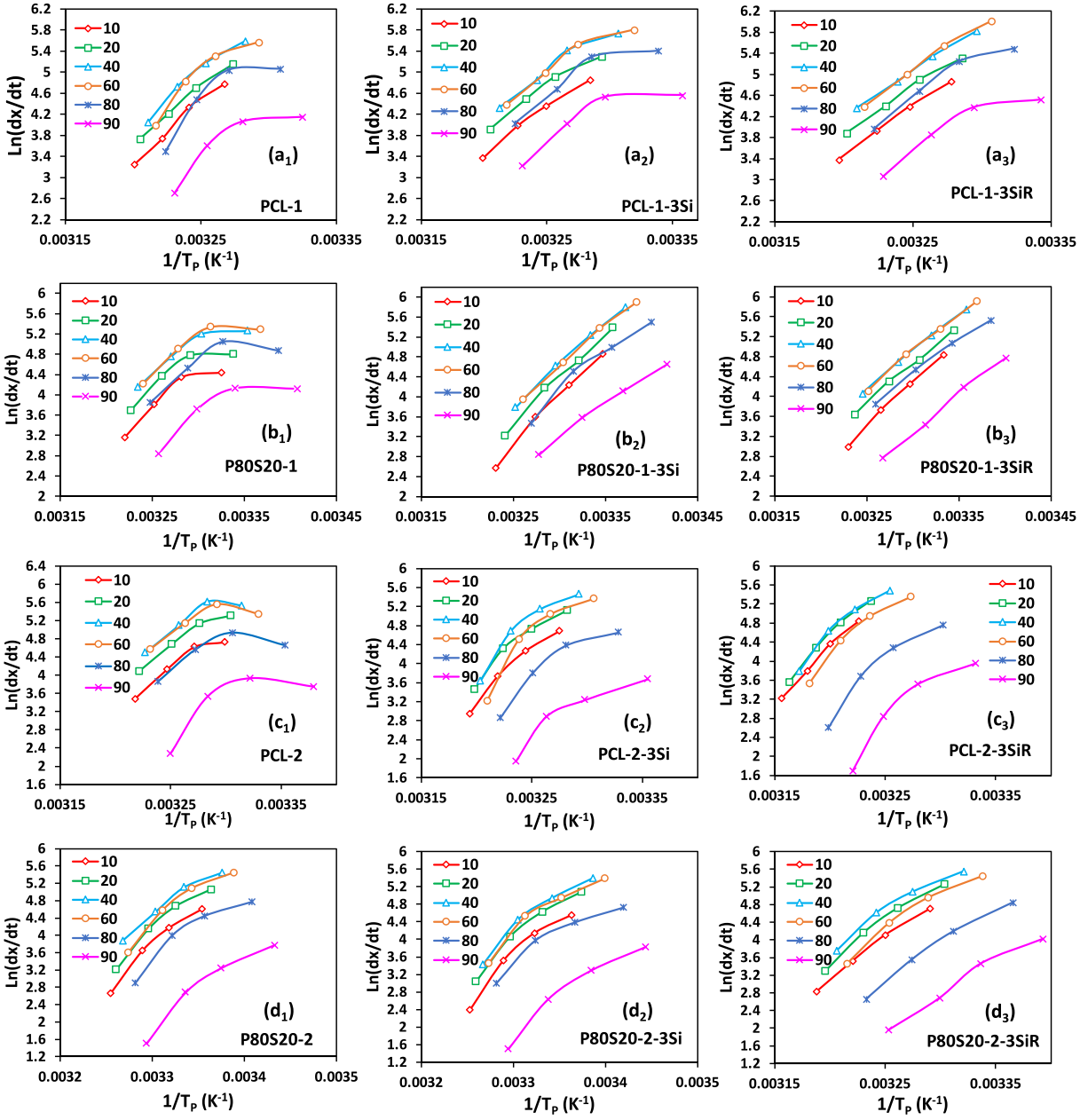

Fig. 7. Plots of ln $(dx/dt)_{x,i}$ vs $1/T_x$ in different crystallinity degrees for (a_1, a_2, a_3) virgin PCL-1, PCL-1-3Si, and PCL-1-3SiR, (b_1, b_2, b_3) P80S20-1, P80S20-1-3Si, and P80S20-1-3SiR, (c_1, c_2, c_3) virgin PCL-2, PCL-2-3Si, and PCL-2-3SiR, (d_1, d_2, d_3) P80S20-2, P80S20-2-3Si, and P80S20-2-3SiR.

nanoparticles is small. For P80S20-2-based nanocomposites, ΔE_C decreased at lower $X_C(T)$, while it increased at higher $X_C(T)$ due to the incorporation of Si and SiR.

3.2. Discussion

By adding Si and SiR nanoparticles to PCL-1 and PCL-2 samples, in general, at all cooling rates (unless 2 K/min for PCL-2-3Si), the Z_{t2} and Z_t values reduce and the $\tau_{1/2}$ value increases (see Tables 1 and 2). It means that adding 3 phr of hydrophilic and hydrophobic nanosilica to PCL-1 and PCL-2 samples leads to a lower crystallization rate of PCL.

However, the incorporation of Si and SiR into P80S20 blends has yielded interesting data. The addition of Si to P80S20-1 leads to the deceleration of crystallization kinetics of PCL at two lower cooling rates (2 and 5 K/min) compared to P80S20-1, while it accelerates it at the two higher cooling rates (10 and 20 K/min). However, the effect of Si on P80S20-2 is vice versa. Indeed, the incorporation of Si to P80S20-2 accelerates the crystallization rate at two lower cooling rates, while slowing down it at two higher rates. With the addition of SiR, the Z_{t2} of P80S20-1-3SiR increased at all cooling rates compared to P80S20-1, which means speeding up the crystallization rate of P80S20-1 in the presence of SiR. Interestingly, the addition of SiR to P80S20-2 considerably decreases the Z_{t2} at all cooling rates. Indeed, based on the kinetics analysis's result, the crystallization process of PCL in P80S20-1 is considerably accelerated in the presence of the hydrophobic SiR, whereas the hydrophilic Si contributes only slightly to the PCL crystallization process in P80S20-1 (only at higher cooling rates). These reverse effects of Si and SiR on the crystallization kinetics of PCL in PCL/SAN blends are related to the preferential localization of Si/SiR in the biphasic PCL/SAN blends, different influences of silica nanoparticles on the LCST-type phase behavior of PCL/SAN blends and changes in the LCST phase diagram position by altering the PCL molecular weight.

The bulk morphology of cryo-microtomed P80S20-1-3SiR, P80S20-2-3Si, P80S20-2-3SiR, P50S50-1-3Si and P50S50-1-3SiR was studied

Table 7
The values of effective activation energy at constant crystallinity degrees determined by the Friedman equation.

Sample	X_C(T)	ΔE_X	R^2	Sample	X_C(T)	ΔE_X	R^2
PCL-1	10	195.00	0.986	PCL-2	10	131.27	0.923
	20	174.18	0.992		20	125.03	0.952
	40	175.62	0.966		40	104.07	0.823
	60	167.55	0.890		60	67.65	0.645
	80	146.70	0.757		80	55.86	0.520
	90	118.92	0.762		90	83.84	0.565
PCL-1-3Si	10	158.13	0.977	PCL-2-3Si	10	176.79	0.965
	20	118.09	0.979		20	160.37	0.940
	40	121.99	0.974		40	164.31	0.894
	60	119.41	0.937		60	177.58	0.865
	80	90.09	0.843		80	135.14	0.873
	90	86.59	0.801		90	110.53	0.866
PCL-1-3SiR	10	152.28	0.977	PCL-2-3SiR	10	167.05	0.918
	20	143.35	0.979		20	162.51	0.941
	40	141.36	0.974		40	168.83	0.949
	60	148.42	0.937		60	191.94	0.981
	80	125.65	0.843		80	196.07	0.993
	90	105.39	0.801		90	161.68	0.878
P80S20-1	10	101.79	0.992	P80S20-2	10	161.77	0.959
	20	81.87	0.994		20	148.05	0.952
	40	77.65	0.996		40	122.67	0.966
	60	68.78	0.997		60	132.45	0.928
	80	60.23	0.966		80	131.53	0.928
	90	66.95	0.993		90	119.38	0.889
P80S20-1-3Si	10	162.61	0.992	P80S20-2-3Si	10	160.19	0.940
	20	151.73	0.994		20	146.10	0.951
	40	139.55	0.996		40	133.14	0.944
	60	132.72	0.997		60	122.49	0.928
	80	126.60	0.966		80	100.65	0.921
	90	107.64	0.993		90	126.50	0.940
P80S20-1-3SiR	10	147.79	0.996	P80S20-2-3SiR	10	152.18	0.992
	20	129.46	0.997		20	150.08	0.974
	40	124.04	0.998		40	127.72	0.956
	60	125.87	0.996		60	132.44	0.957
	80	111.62	0.993		80	136.12	0.981
	90	126.86	0.996		90	125.43	0.980

by TEM and reported on Fig. 8 and Fig. 9 to illustrate the effects of the nanofiller type and PCL molecular weight on the localization and dispersion state of silica nanoparticles, respectively. As can be found from the images in Fig. 8, the dispersion state of hydrophobic nanosilica (SiR) is better than the one for hydrophilic nanosilica (Si) for both blends containing PCL-1 and PCL-2. Additionally, from Fig. 9, it can be concluded that the SiR dispersion state improves by increasing PCL molecular weight. The presence of smaller silica nanoparticle agglomerates and aggregates can prove these facts. The hydrophilic nature and lower specific surface area of SiR nanoparticles as well as the higher viscosity of the PCL-2-based blends during the melt-compounding process cause better dispersion of hydrophobic nanosilica, especially in the PCL-2-based blends. The dispersion state of nanoparticles has a considerable effect on the PCL crystallization kinetics.

Besides these data, from the TEM images of Figs. 8 and 9, clearly no selective localization for Si and SiR nanoparticles can be perceived. The staining of the cryo-microtomed specimens did not increase the contrast of PCL-rich and SAN-rich domains. However, a closer look at the TEM images shows that the surface has some darker and brighter areas. These areas can be considered as PCL-rich and SAN-rich domains, since these polymers have different mechanical properties. By considering that, no preferential localization for Si and SiR nanoparticles can be perceived in both PCL-1 and PCL-2-based nanocomposites. It is noteworthy that for the TEM image preparation, the cryo-microtomy was done on the samples without any annealing after the melt-compounding process. Indeed, in these samples, Si and SiR nanoparticles are localized in both PCL-rich and SAN-rich regions, as well as the PCL/SAN interface for both PCL molecular weights.

The preferential localization of Si and SiR nanoparticles at the interface of PCL and SAN-rich domains was reported in our previous work according to the theoretically calculated wettability parameters of hydrophilic Si and hydrophobic SiR in PCL/SAN blends (Mohtaramzadeh et al., 2020). However, the microscopic observations on the samples without annealing after melt-compounding mostly show non-selective localization of nanoparticles. In our previous paper, it was demonstrated that the hydrophilic nanosilica particles migrate to the SAN-rich domains by annealing the samples, owing to the higher interfacial tensions of PCL/Si and SAN/Si pairs compared to the interfacial tension of PCL/SAN pair. Both theoretical calculation of interfacial tensions and TEM images on the annealed samples supported the Si nanoparticles migration to the SAN-rich domains during the DSC tests (Mohtaramzadeh et al., 2020). In contrast, the hydrophobic nanosilica is preferentially localized at PCL-rich and SAN-rich domains as well as PCL/SAN interface (supported by both theoretical calculations and experimental evidence) (Mohtaramzadeh et al., 2020). During the non-isothermal DSC experiments, the samples were heated to 130 °C to erase the thermal history. At this segment of the DSC test, the entrance to the phase-separated region of LCST phase diagram and the Si nanoparticle migration to the SAN-rich domains would probably happen. Considering different cooling rates of the DSC tests, the occurrence of these kinetic-controlled phenomena will be more noticeably observed at lower cooling rates, i.e., 2 and 5 °C/min.

In addition to the nanosilica particle migration during the non-isothermal DSC test, the position of the LCST-type phase diagram of PCL/SAN blends has a profound impact on the crystallization kinetics of the PCL phase. Indeed, the amount of dissolved amorphous SAN chains that can retard the PCL-phase crystallization is determined by the PCL/SAN phase separation and mutual dissolution. It is affected by the LCST phase diagram position and the non-isothermal DSC ramp rate. According to our previous works, the position of the phase boundary of the PCL/SAN LCST-type phase diagram changes by altering the PCL molecular weight and adding hydrophilic and hydrophobic nanosilica (Maghoul et al., 2023; Khadivi et al., 2023; Mohtaramzadeh et al., 2020). In one of these works, it has shown that the addition of SiR nanoparticles to PCL/SAN blend causes the shift of the equilibrium LCST phase diagram to higher temperatures. Contrary to the compatibilization effect of SiR nanofiller on the PCL/SAN phase behavior, the presence of hydrophilic nanosilica, Si, shifted the phase diagram to lower temperatures and decreased the miscibility window area (Maghoul et al., 2023).

In another work of our group on the non-isothermal crystallization kinetics of PCL in PCL/SAN blends containing PCL grades with different molecular weights, it was shown that the PCL crystallization in the blend with lower molecular weight of PCL was comparatively easier (Khadivi et al., 2023). In that work, it was found that the plausible reason for the easier crystallization in P80S20-1 blend was the presence of the larger amount of dissolved SAN chains in the PCL-rich domains, which was induced by phase separation during DSC experiment at higher temperatures. In contrast, the LCST-type phase diagram for P80S20-2 was probably shifted to higher temperatures and during the heating segment of the DSC test, the sample did not succeed in entering the phase-separated region of the LCST phase diagram (Khadivi et al., 2023). More dissolved amorphous SAN chains in the P80S20-2 blend brought about higher activation energy of PCL crystallization. Better compatibility of PCL and SAN phases in PCL-1 and PCL-2-based systems can be clarified by comparing the SEM images of these mixtures, which were prepared by examining the cryo-microtomed surfaces. Fig. 10 and Figure S2 (in the supporting information) demonstrate the lower size of rough areas that are related to the SAN-rich domains. Contrary to the PCL-1-based systems in Fig. 10, no visible rough areas can be discerned on the SEM images of PCL-2-based mixtures, confirming the higher miscibility of PCL and SAN in the blend containing the PCL polymer with higher molecular weight.

Considering the above evidence can help someone interpret the obtained data showing opposite effects of Si and SiR on the PCL crystallization kinetics in PCL-1 and PCL-2-based blends. For the SiR nanosilica

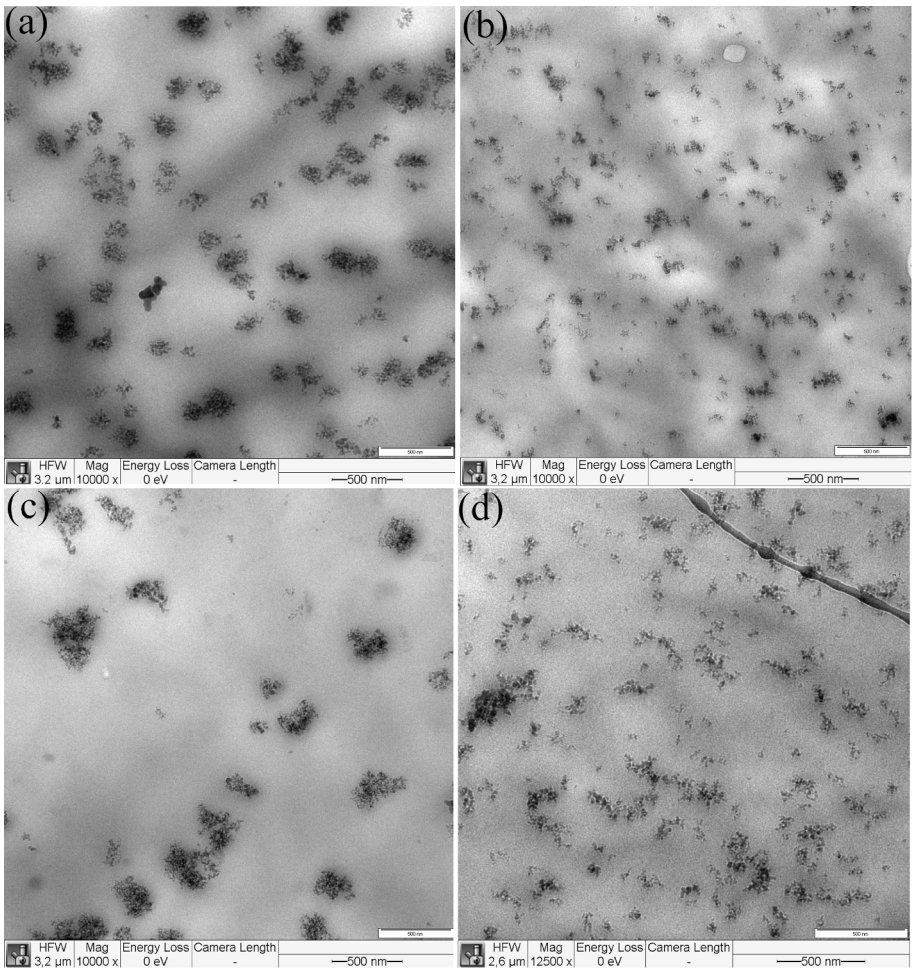

Fig. 8. TEM image of: (a) P80S20-2-3Si, (b) P80S20-2-3SiR, (c) P50S50-1-3Si and (d) P50S50-1-3SiR.

influence on the crystallization of P80S20-1 and P80S20-2 blends, it should be kept in mind that SiR nanoparticles have no selective localization state in PCL/SAN blends and LCST-type phase diagram is most likely shifted to higher temperatures in PCL-2-based blends. As a direct result, P80S20-2-3SiR does not enter the phase-separated region during the heating segment of the DSC experiment. In contrast, P80S20-1-3SiR nanocomposite most probably enters the phase-separated region during the examination. Therefore, less amount of dissolved SAN chains alongside PCL chains during crystallization makes the poisoning SAN effect less strong. By that, SiR nanoparticles with good dispersion state attain the opportunity to accelerate the PCL crystallization process by providing larger heterogeneous nucleation sites. Thus, SiR nanofiller accelerates PCL crystallization in P80S20-1 and oppositely retards PCL crystallization in P80S20-2 blend.

For the adverse effects of the hydrophilic nanosilica on the PCL crystallization kinetics of PCL-1 and PCL-2-based blends, which also depend on the DSC cooling rate, four notable points should be considered. First of all, Si nanoparticles do not disperse as well as SiR nanofiller in PCL/SAN blends. Second, hydrophilic nanosilica thermodynamically prefers to migrate to the SAN-rich domains. Third, Si nanofiller does not improve better PCL/SAN miscibility like hydrophobic nanosilica. Fourth, the PCL-2-based blend has higher compatibility than the PCL-1-based mixture. As a result, the LCST-phase diagram of PCL/SAN will be positioned at a lower temperature for P80S20-1-3Si. During the first segments of the DSC experiment, the nanocomposite enters the phase-separated region. By the occurrence of PCL/SAN phase separation, less amount of dissolved SAN in the PCL-rich phase causes a weaker retardation effect on the crystallization. Therefore, Si nanoparticles will be successful to accelerate the PCL crystallization at cooling rates of 10 and 20 K/min. While, at lower cooling rates (2 and 5 K/min), the preferential migration of hydrophilic nanosilica to the SAN-rich phase makes the acceleration effect of nanoparticles less intensified. Thus, a retardation effect for Si in P80S20-1-3Si is observed at lower cooling rates of 2 and 5 K/min.

For P80S20-2-3Si nanocomposite, the PCL polymer has a higher molecular weight. In this blend, PCL and SAN have higher compatibility. However, Si nanoparticles do not shift the LCST-type phase diagram to higher temperatures like SiR ones. As a direct result, PCL/SAN phase separation cannot happen at higher cooling rates of 10 and 20 K/min. Indeed, a higher amount of dissolved SAN chains diminishes the PCL crystallization rate in the P80S20-2-3Si sample at higher cooling rates. Contrary to that, the P80S20-2-3Si nanocomposite most likely encounters the phase separation to some extent at lower cooling rates of 2 and 5 K/min. Therefore, the phase separation of amorphous SAN chains provides the opportunity for silica nanoparticles with a better dispersion state in P80S20-2-3Si than in P80S20-1-3Si to assist the PCL crystallization process.

Following the aim of this work, it has been shown that the non-isothermal crystallization behavior is a complex phenomenon in the semi-crystalline/amorphous polymeric systems containing nanoparticles. The crystallization kinetics in these systems has a significant effect on the product's final properties. The findings clarify that different factors like the system phase behavior, the nanoparticle preferential migration to one of the phases, the molecular weight of the polymeric components and the position of the miscibility window noticeably influence the crystallization kinetics.

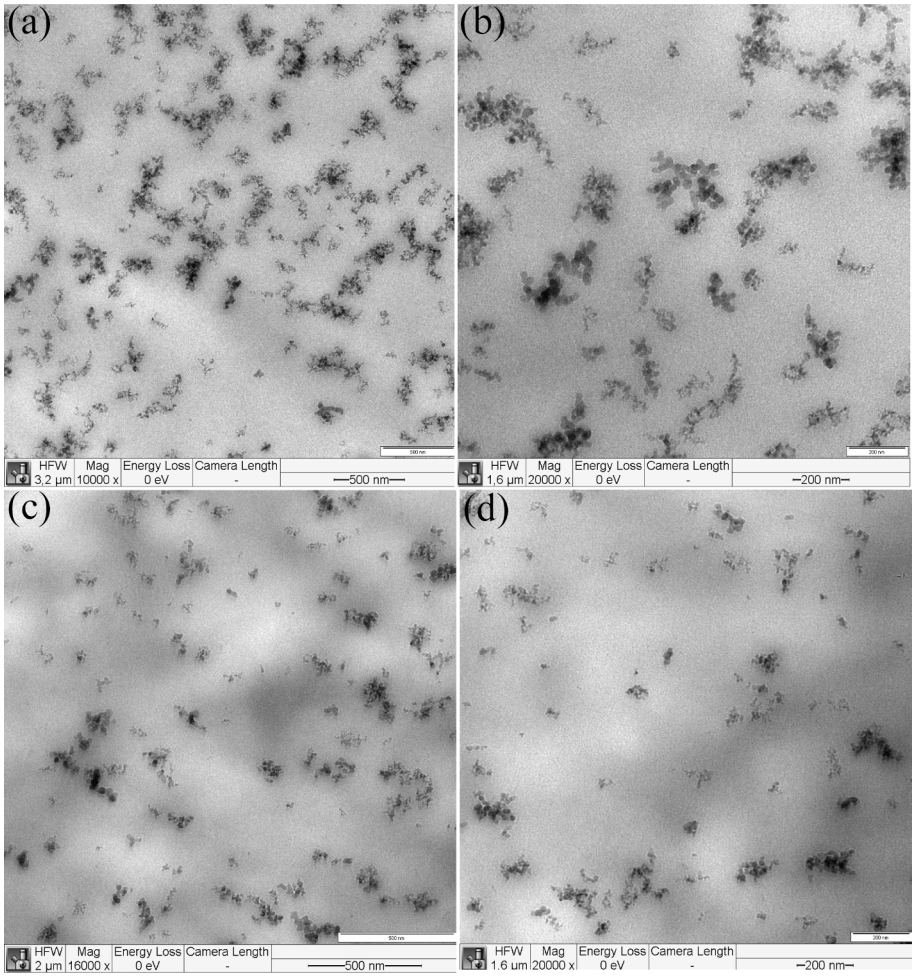

Fig. 9. TEM image of: (a)-(b) P80S20-1-3SiR and (c)-(d) P80S20-2-3SiR.

4. Conclusions

In this work, the semicrystalline/amorphous PCL/SAN mixtures, with LCST-type phase diagram up above the crystallization temperature of PCL, were chosen to study the effects of PCL molecular weight and nanosilica type on the non-isothermal crystallization kinetics. The crystallization kinetics variables and activation energy of PCL were determined by fitting theoretical models on the experimental data including Avrami, Jeziorny, Ozawa, Mo, Kissinger and Friedman models. Among different applied theoretical models, the best fitting of the experimental data is obtained for the Avrami, Jeziorny, Mo and Kissinger models. The largest R^2s are attained for the determination of Z_{t2} and Z_{c2} (considering a three-stage crystallization), $F(T_C)$ and E_C. These kinetic variables are the most useful parameters for showing the changes in the PCL crystallization rate against the PCL molecular weight, nanosilica type and DSC cooling rate. According to these data, the following results are concluded:

While the presence of both hydrophilic and hydrophobic nanosilica fillers has a retardation effect on the PCL crystallization kinetics, the presence of these nanoparticles in the PCL/SAN blends affects the PCL crystallization kinetics through opposite trends depending on the PCL molecular weight, nanosilica type and DSC cooling rate. The hydrophobic nanosilica accelerates the PCL crystallization in the PCL/SAN blend containing PCL with lower molecular weight, regardless of the DSC cooling rate. In contrast, this nanofiller retards the PCL crystallization for the blend based on the higher molecular weight PCL. The plausible reasons for these opposite trends are the probable shift of the LCST phase diagram by increasing the PCL molecular weight, relatively better dispersion state and no preferential localization state of this type of nanosilica. Nonetheless, the influences of hydrophilic nanosilica on the PCL crystallization in the PCL/SAN mixture also depend on the cooling rate of the DSC test. The Si nanoparticles decrease the PCL crystallization rate at a lower DSC ramp rate, while these increase crystallizations at higher cooling rates, albeit for the PCL/SAN blend including lower molecular weight PCL. For the blend based on the higher molecular weight PCL, the Si effects on the PCL crystallization are totally opposite. As mentioned, the changes in the LCST phase diagram induced by the nanosilica presence and PCL molecular weight, selective migration of nanosilica during the test and nanosilica dispersion state are the important factors to cause the opposite trends in the crystallization behavior of PCL in the PCL/SAN blends. Overall, according to the findings, it can be concluded that the non-isothermal crystallization of polymers in hybrid systems with a special phase behavior like the one studied here is a complex phenomenon, that is impacted by several factors. Each of these factors can alter the crystallization rate in different ways. In industrial-scale production of similar systems, these factors should be considered to optimize the crystallization and final properties of the products.

CRediT authorship contribution statement

Samaneh Salkhi Khasraghi: Conceptualization, Methodology, Investigation, Resources, Visualization, Software, Writing – original draft. **Hanieh Khonakdar:** Conceptualization, Methodology, Investigation, Resources, Visualization, Software, Writing – original draft. **Farkhondeh Hemmati:** Investigation, Resources, Writing – review &

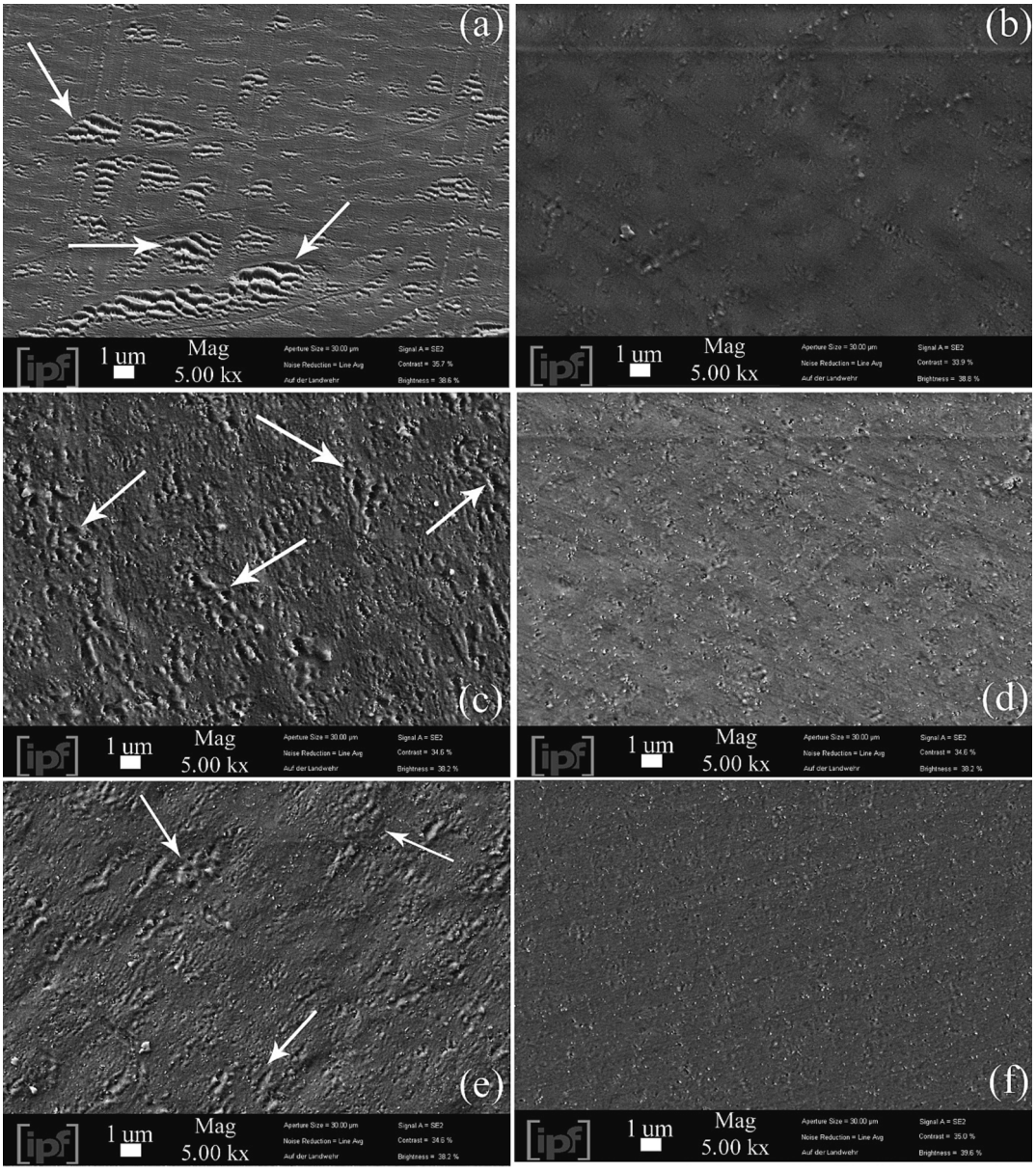

Fig. 10. SEM image of the cryo-microtomed surface of: (a) P80S20-1, (b) P80S20-2, (c) P80S20-1-Si3, (d) P80S20-2-3Si, (e) P80S20-1-3SiR and (f) P80S20-2-3SiR. The white arrows mark the SAN-rich domains.

editing. **Sara Zarei:** Methodology, Investigation, Resources, Visualization, Software. **Fatemeh Sadat Miri:** Methodology, Investigation, Resources, Visualization, Software. **Marcos A.L. Nobre:** Investigation, Resources, Writing – review & editing. **Hossein Ali Khonakdar:** Investigation, Resources, Writing – review & editing.

Declaration of competing interest

The authors declare that they have no known competing financial interests or personal relationships that could have appeared to influence the work reported in this paper.

Appendix A. Supplementary material

Supplementary data to this article can be found online at https://doi.org/10.1016/j.arabjc.2023.105522.

References

Albertsson, A.-C., Varma, I.K., 2002. Aliphatic polyesters: Synthesis, properties and applications. Degradable Aliphatic Polyesters 1–40.

Arshian, M., Estaji, S., Tayouri, M.I., Mousavi, S.R., Shojaei, S., Khonakdar, H.A., 2023. Poly (lactic acid) films reinforced with hybrid zinc oxide-polyhedral oligomeric silsesquioxane nanoparticles: morphological, mechanical, and antibacterial properties. Polym. Adv. Technol. 34 (3), 985–997.

Asadinezhad, A., Khonakdar, H.A., Häußler, L., Wagenknecht, U., Heinrich, G., 2014. Crystallization and melting behavior of poly (ethylene succinate) in presence of graphene nanoplatelets. Thermochim Acta 586, 17–24.

Avrami, M., 1940. Kinetics of phase change. II transformation-time relations for random distribution of nuclei. J. Chem. Phys. 8 (2), 212–224.

Azizli, M.J., Mokhtary, M., Khonakdar, H.A., Goodarzi, V., 2020. Compatibilizer/graphene/carboxylated acrylonitrile butadiene rubber (XNBR)/ethylenepropylenediene monomer (EPDM) nanocomposites: Morphology, compatibility, rheology and mechanical properties. J. Appl. Polym. Sci. 137 (43).

Choi, J., Kwak, S.-Y., 2004. Architectural effects of poly (ε-caprolactone) s on the crystallization kinetics. Macromolecules 37 (10), 3745–3754.

Choolaei, M., Goodarzi, V., Khonakdar, H.A., Jafari, S.H., Seyfi, J., Saeb, M.R., Häußler, L., Boldt, R., 2017. Influence of graphene oxide on crystallization behavior and chain folding surface free energy of poly (vinylidenefluoride-co-hexafluoropropylene). Macromol. Chem. Phys. 218 (19), 1700103.

Crosby, A.J., Lee, J.Y., 2007. Polymer nanocomposites: the "nano" effect on mechanical properties. Polym. Rev. 47 (2), 217–229.
Dhanvijay, P.U., Shertukde, V.V., Kalkar, A.K., 2012. Isothermal and nonisothermal crystallization kinetics of poly (ϵ-caprolactone). J. Appl. Polym. Sci. 124 (2), 1333–1343.
Ebadi-Dehaghani, H., Barikani, M., Khonakdar, H.A., Jafari, S.H., 2015. Microstructure and non-isothermal crystallization behavior of PP/PLA/clay hybrid nanocomposites. J. Therm. Anal. Calorim. 121, 1321–1332.
Fakhri, V., Monem, M., Mir Mohamad Sadeghi, G., Khonakdar, H.A., Goodarzi, V., Karimpour-Motlagh, N., 2021. Impact of poly (ε-caprolactone) on the thermal, dynamic-mechanical and crystallization behavior of polyvinylidene fluoride/poly (ε-caprolactone) blends in the presence of KIT-6 mesoporous particles. Polym. Adv. Technol. 32 (11), 4424–4439.
Friedman, H.L., 1964. Kinetics of thermal degradation of char-forming plastics from thermogravimetry. Application to a phenolic plastic. J. Polym. Sci. Part c: Polym. Symposia.
Ghafouri, S.E., Mousavi, S.R., Khakestani, M., Mozaffari, S., Ajami, N., Khonakdar, H.A., 2022. Electrospun nanofibers of poly (lactic acid)/poly (ε-caprolactone) blend for the controlled release of levetiracetam. Polym. Eng. Sci. 62 (12), 4070–4081.
Goodarzi, V., Jafari, S.H., Khonakdar, H.A., Monemian, S.A., Hässler, R., Jehnichen, D., 2009. Nonisothermal crystallization kinetics and determination of surface-folding free energy of PP/EVA/OMMT nanocomposites. J. Polym. Sci. B 47 (7), 674–684.
Hemmati, F., Garmabi, H., Modarress, H., 2014. Effects of organoclay on the compatibility and interfacial phenomena of PE/EVA blends with UCST phase behavior. Polym. Compos. 35 (12), 2329–2342.
Higgins, J.S., Tambasco, M., Lipson, J.E., 2005. Polymer blends; stretching what we can learn through the combination of experiment and theory. Prog. Polym. Sci. 30 (8–9), 832–843.
Hosseiny, S.M., Jafari, S.H., Khonakdar, H.A., Hemmati, F., Kalaee, M.R., 2020. A correlation between morphology and mechanical performance of injected-molded PE/EVA/clay nanocomposites: Insight into phase miscibility and interfacial phenomena. J. Appl. Polym. Sci. 137 (45), 49401.
Jafari, S.M.A., Khajavi, R., Goodarzi, V., Kalaee, M.R., Khonakdar, H.A., 2019. Nonisothermal crystallization kinetic studies on melt processed poly (ethylene terephthalate)/polylactic acid blends containing graphene oxide and exfoliated graphite nanoplatelets. J. Appl. Polym. Sci. 136 (23), 47569.
Jana, R., Cho, J.W., 2010. Non-isothermal crystallization of poly (ε-caprolactone)-grafted multi-walled carbon nanotubes. Compos. A Appl. Sci. Manuf. 41 (10), 1524–1530.
Jeziorny, A., 1978. Parameters characterizing the kinetics of the non-isothermal crystallization of poly (ethylene terephthalate) determined by DSC. Polymer 19 (10), 1142–1144.
Kalva, S.N., Dalvi, Y.B., Khanam, N., Varghese, R., Ahammed, I., Augustine, R., Hasan, A., 2023. Air-jet spun PHBV/PCL blend tissue engineering scaffolds exhibit improved mechanical properties and cell proliferation. Results Mater., 100415
Khadivi, E., Khonakdar, H., Salkhi Khasraghi, S., Hemmati, F., Salahshoori, I., Ehsani, M., Arnhold, K., Khonakdar, H.A., 2023. Correlation between non-isothermal crystallization kinetics and morphology in poly (ε-caprolactone)/poly (styrene-co-acrylonitrile) blends considering the blend phase behavior: Effects of poly (ε-caprolactone) molecular weight. J. Appl. Polym. Sci. e54384.
Kissinger, H.E., 1956. Variation of peak temperature with heating rate in differential thermal analysis. J. Res. Natl. Bur. Stand 57 (4), 217–221.
Li, Y., Cheng, H., Yu, M., Han, C., Shi, H., 2022. Blends of biodegradable poly (ε-caprolactone) and sustainable poly (propylene carbonate) with enhanced mechanical and rheological properties. Colloid Polym. Sci. 1–10.
Limwanich, W., Phetsuk, S., Meepowpan, P., Kungwan, N., Punyodom, W., 2016. Kinetics studies of non-isothermal melt crystallization of poly (ε-caprolactone) and poly (L-lactide). Chiang Mai J. Sci 43, 329–338.
Luyten, M., Bögels, E., Van Ekenstein, G.A., Ten Brinke, G., Bras, W., Komanschek, B., Ryan, A., 1997. Morphology in binary blends of poly (vinyl methyl ether) and ϵ-caprolactone-trimethylene carbonate diblock copolymer. Polymer 38 (3), 509–519.
Madbouly, S.A., 2011. Nonisothermal crystallization kinetics of miscible blends of polycaprolactone and crosslinked carboxylated polyester resin. J. Macromol. Sci. Part B 50 (3), 427–443.
Madbouly, S.A., Ougizawa, T., 2004. Isothermal crystallization of poly (ε-caprolactone) in blend with poly (styrene-co-acrylonitrile): influence of phase separation process. Macromol. Chem. Phys. 205 (14), 1923–1931.
Madbouly, S.A., Abdou, N.Y., Mansour, A.A., 2006. Isothermal crystallization kinetics of poly (ε-caprolactone) with tetramethyl polycarbonate and poly (styrene-co-acrylonitrile) blends using broadband dielectric spectroscopy. Macromol. Chem. Phys. 207 (11), 978–986.
Maghoul, A., Khasraghi, S.S., Khonakdar, H., Mousavi, S.R., Hemmati, F., Kühnert, I., Leuteritz, A., Nobre, M.A., Khonakdar, H.A., 2023. Thermodynamically-equilibrium LCST phase diagram of PCL/SAN mixtures determined by thermal analysis: opposing effects of hydrophilic and hydrophobic silica nanoparticles. Thermochim Acta 724, 179501.
Maiti, S., Jacob, J., 2017. Nonisothermal crystallization and microstructural behavior of poly (ε-caprolactone) and granular tapioca starch-based biocomposites. Int. J. Polym. Anal. Characterization 22 (3), 222–236.
Mdletshe, T.S., Mishra, S.B., Mishra, A.K., 2015. Studies on the effect of silicon carbide nanoparticles on the thermal, mechanical, and biodegradation properties of poly (caprolactone). J. Appl. Polym. Sci. 132 (26).
Moeinifar, E., Otadi, M., Seyfi, J., Khonakdar, H.A., 2020. Study on the effects of polyhedral oligomeric silsesquioxane on compatibility, crystallization behavior and thermal stability of polylactic acid/polycaprolactone blends. Polym. Bull. 77, 585–598.
Mohamed, R.M., Yusoh, K., 2016. A review on the recent research of polycaprolactone (PCL). Adv. Mat. Res. 1134, 249–255.
Mohtaramzadeh, Z., Hemmati, F., Kasbi, S.F., Goodarzi, V., Arnhold, K., Khonakdar, H. A., 2020. Structure-properties correlations in poly (ε-caprolactone)/poly (styrene-co-acrylonitrile)/nanosilica mixtures: Interrelationship among phase behavior, morphology and non-isothermal crystallization kinetics. Polym. Test. 89, 106593.
Naziri, A.A., Khonakdar, H.A., Hemmati, F., Jafari, S.H., Ehsani, M., 2019. Rheologically determined phase diagram of poly (ε-caprolactone)/poly (styrene-co-acrylonitrile) blends: Role of ramp rate in dynamic measurements. J. Appl. Polym. Sci. 136 (28), 47750.
Naziri, A.A., Ehsani, M., Khonakdar, H.A., Hemmati, F., Jafari, S.H., 2020. Spherical nanoparticle effects on the lower critical solution temperature phase behavior of poly (ε-caprolactone)/poly (styrene-co-acrylonitrile) blends: separation of thermodynamic aspects from kinetics. J. Appl. Polym. Sci. 137 (19), 48679.
Ozawa, T., 1971. Kinetics of non-isothermal crystallization. Polymer 12 (3), 150–158.
Qian, J., Xiao, Z., Dong, L., Tang, D., Li, M., Yang, Q., Huang, Y., Liao, X., 2016. Morphology and crystallization behavior of PCL/SAN blends containing nanosilica with different surface properties. J. Appl. Polym. Sci. 133 (43).
Salkhi Khasraghi, S., Momenilandi, M., Shojaei, A., 2022. Tire tread performance of silica-filled SBR/BR rubber composites incorporated with nanodiamond and nanodiamond/nano-SiO_2 hybrid nanoparticle. Diam. Relat. Mater. 126, 109068.
Schulze, K., Kressler, J., Kammer, H., 1993. Phase behaviour of poly (ϵ-caprolactone)/(polystyrene-ran-acrylonitrile) blends exhibiting both liquid-liquid unmixing and crystallization. Polymer 34 (17), 3704–3709.
Su, C.-C., Lin, J.-H., 2004. Ringed spherulites in ternary polymer blends of poly (ε-caprolactone), poly (styrene-co-acrylonitrile), and polymethacrylate. Colloid Polym. Sci. 283, 182–193.
Svoboda, P., Kressler, J., Chiba, T., Inoue, T., Kammer, H.W., 1994. Light-scattering and TEM analyses of virtual upper critical solution temperature behavior in PCL/SAN blends. Macromolecules 27 (5), 1154–1159.
Svoboda, P., Keyzlarová, L., Sáha, P., Rybnikář, F., Chiba, T., Inoue, T., 1999. Spinodal decomposition and succeeding crystallization in PCL/SAN blends. Polymer 40 (6), 1459–1463.
Svoboda, P., Svobodova, D., Chiba, T., Inoue, T., 2008. Competition of phase dissolution and crystallization in poly (ε-caprolactone)/poly (styrene-co-acrylonitrile) blend. Eur. Polym. J. 44 (2), 329–341.
Tuancharoensri, N., Ross, G.M., Kongprayoon, A., Mahasaranon, S., Pratumshat, S., Viyoch, J., Petrot, N., Ruanthong, W., Punyodom, W., Topham, P.D., 2023. In situ compatibilized blends of PLA/PCL/CAB melt-blown films with high elongation: investigation of miscibility, morphology, crystallinity and modelling. Polymers 15 (2), 303.
Woodruff, M.A., Hutmacher, D.W., 2010. The return of a forgotten polymer—Polycaprolactone in the 21st century. Prog. Polym. Sci. 35 (10), 1217–1256.
Xu, P., Tan, S., Niu, D., Wang, Q., Liu, T., Yang, W., Ma, P., 2023. Effect of temperatures on stress-induced structural evolution and mechanical behaviors of polyglycolic acid/polycaprolactone blends. Polymer 283, 126239.
Zhang, Y., Wu, Y., Yang, M., Zhang, G., Ju, H., 2021. Thermal stability and dynamic mechanical properties of poly (ε-caprolactone)/chitosan composite membranes. Materials 14 (19), 5538.